On a Coupled Aerodynamic and Aeroacoustic Shape Optimization Framework for a 2D Airfoil

Master Thesis

Faculty of Aerospace Engineering

Luigi Manni

Delft University of Technology

TU Delft

On a Coupled Aerodynamic and Aeroacoustic Shape Optimization Framework for a 2D Airfoil

Master Thesis

by

Luigi Manni

Student number
4911334

TU Delft Supervisor:	Prof. Roeland De Breuker
IST Supervisors:	Prof. Fernando Lau, Prof. Frederico Afonso
Project Duration:	October, 2022 - May, 2024
Faculty:	Faculty of Aerospace Engineering, TU Delft

Preface

This thesis marks the end of a long journey for me, made of many new experiences, new friends and new places, for which I will be forever grateful. I would like now to express my appreciation to all those who supported me in these years and contributed to this achievement.

First of all, I would like to thank my thesis supervisors who made this work possible. Thank you to Dr. Ir. Roeland De Breuker, for his guidance and availability in allowing my exchange period in Lisbon. I also owe a heartfelt thank you to my Portuguese supervisors, Professor Fernando Lau and Professor Frederico Afonso, for their friendly and continuous support and patience. You have welcomed me in the department very warmly, inspired my research and helped me throughout my high's and low's, for which I am extremely grateful for.

Besides my academic achievements, the past years in Delft allowed me to meet amazing people I am proud to call my friends. I am so thankful for all we have been through together: the special moments and the routine, the coffees and the dinners, the bikes and the trains, the discussions and new ideas, the laughs and the tears. Thanks to you I was able to grow lighthearted and with an open mind, and you made my time in the Netherlands an unforgettable period of my life. I feel truly lucky to have crossed paths with each of you, and no matter the distance, we will always stay close.

A special mention goes to two of my friends who particularly impacted my academic journey. Firstly to Uncio: we met on the first day in Delft and since then we could never stay apart. Thank you for your brotherly friendship and for always being there for me with your spontaneity. Secondly, I would like to thank Gri: from the first derivatives in Rome, to the last thesis revisions from overseas, I never missed your support, and it means the world to me.

Finally, I would like to express my gratitude to my parents and my brother for their unconditional support and love. I cannot thank you enough for making me the person I am today, for the values you have taught me and the strength you constantly transmit me even from afar. Without you, nothing would have been possible.

Luigi Manni
Delft, May 2024

Abstract

In recent years, aircraft noise has emerged as a pressing concern within aeronautics, due to its adverse health impacts and the increasing annoyance experienced by affected populations. Factors such as rapid urbanization, urban encroachment resulting in closer proximity of residential areas to airports, and the continuous growth of air traffic have exacerbated this issue. Current approaches to mitigate aircraft noise primarily focus on integrating additional components rather than optimizing the airfoil profile a priori.

This thesis aims to actively address this challenge by developing a coupled aerodynamic and aeroacoustic shape optimization framework tailored for a 2D airfoil. The primary objective is to minimize trailing edge noise, identified as one of the dominant noise generating mechanisms during approach and landing, while simultaneously maximizing aerodynamic performance. The solving strategy combines an aerodynamic solver with a state-of-the-art wall pressure spectrum model and Amiet's trailing edge noise (TEN) model, whose inputs are boundary layer parameters extracted from the aerodynamic evaluation.

The efficacy of both lower fidelity (XFOIL) and higher fidelity (Reynolds-Averaged Navier Stokes (RANS)) aerodynamic solvers is evaluated. The airfoil is optimized at different points of the flight envelope: for maximum lift-to-drag ratio during cruise and for minimum trailing edge noise during landing.

Results demonstrate that the genetic algorithm (NSGA-II) optimization framework yields promising airfoil shapes and reliable outcomes at a computationally feasible cost. Many optimizations with varying generations and population sizes are ran: remarkably, the results consistently showcase well-defined Pareto fronts, with superior definition observed particularly at a population size of 200.

The lower fidelity solver proves particularly effective in the landing scenario, while it shows limitations for higher Mach numbers. In this view, the RANS code is necessary for capturing flow phenomena at cruise speeds, and notably, it also provides convincing results in terms of aeroacoustic prediction during landing phase.

In general, this research highlights the potential for significant advancements in designing optimal airfoils for aerodynamic performance and TEN.

Contents

List of Figures

List of Tables

Nomenclature

Abbreviations

Abbreviation	Definition
AD	Automatic Differentiation
AoA	Angle of Attack
ASO	Aerodynamic Shape Optimization
CAA	Computational Aero Acoustics
CFD	Computational Fluid Dynamics
CST	Class Shape Transformation
DES	Detached Eddy Simulation
DoE	Design of Experiment
DNS	Direct Numerical Simulation
FFD	Free Form Deformation
FWH	Ffowcs Williams-Hawkings
GAN	Generative Adversarial Network
GP	Gaussian Process
ISA	International Standard Atmosphere
LHS	Latin Hypercube Sampling
LE	Leading Edge
LES	Large Eddy Simulation
LF	Low Fidelity
MDO	Multidisciplinary Design Optimization
MF	Multi Fidelity
MFM	Multi Fidelity Model
ML	Machine Learning
MUAS	Maximum Uncertainty Adaptive Sampling
NSGA-II	Non Dominated Sorted Genetic Algorithm
PARSEC	Parameterized Sections
PINN	Physically Informed Neural Network
POD	Proper Orthogonal Decomposition
RANS	Reynolds Averaged Navier Stokes
RSM	Response Surface Model
ROM	Reduced Order Model
SNG	Stochastic Noise Generation
SM	Surrogate Model
TE	Trailing Edge
URANS	Unsteady Reynolds Averaged Navier Stokes

Symbols

Latin Symbols

Symbol	Definition	Unit
C_D	Drag coefficient	–
C_L	Lift coefficient	–
C_p	Pressure coefficient	–
D	Drag force	[N]
L	Lift force	[N]
M	Mach number	–
Re	Reynolds number	–
V	Velocity	[m/s]
c	Airfoil chord	[m]
h	Altitude	[m]
p	Static pressure	[Pa]
q	Dynamic pressure	[Pa]
x	Horizontal coordinate	[m]
y	Vertical coordinate	[m]
y^+	Dimensionless wall distance	–
$\mathbf{X}$	Design variable vector	–
Greek Symbols		
α	Angle of attack	°
Γ	Control surface	–
Δ	Difference	–
μ	Kinematic viscosity	[m^2/s]
ρ	Density	[kg/m^3]

1

Introduction

1.1. Motivation

Following the increase of air traffic in the past years, airplane noise pollution has become a growing concern, particularly in areas near airports, where residents are regularly exposed to loud airplane noise. Urbanization and population growth have led to an increased pressure for the expansion of airports and the growth of cities, causing many residents to live in closer proximity to airports. This means that more and more people are being exposed to loud airplane noise on a regular basis: this noise can disrupt sleep and quality of life [1], and has been linked to a variety of health problems, including hypertension [2], cardiovascular disease (see Fig. 1.1), and cognitive impairment in children [3]. Additionally, noise pollution in populated areas can have economic consequences, affecting property values [4].

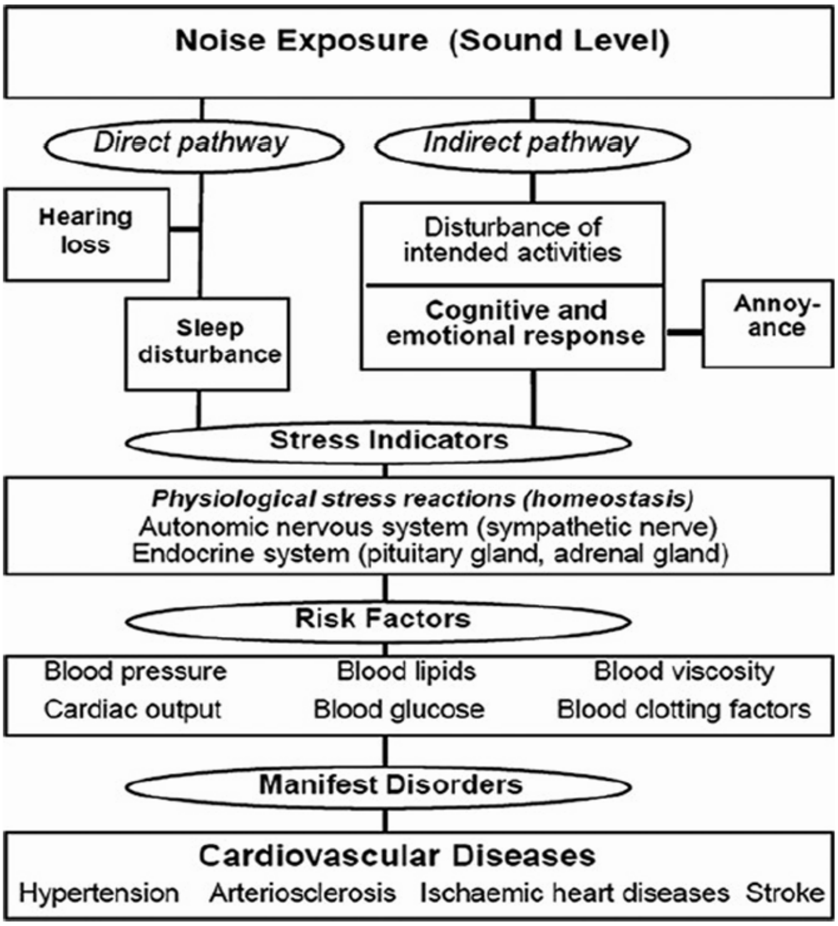

Figure 1.1: Pathways from noise exposure to cardiovascular disease [5].

According to the United Nations, the predictions indicate that urban populations, which constituted 54% in 2014, are expected to rise to 66% by 2050 [6]. While originally, airports were situated far from urban centers to minimize noise impact, the urbanization phenomenon has led to airports being increasingly surrounded by growing urban populations. This urban encroachment into airport areas has heightened the exposure of residents to aircraft noise.

Furthermore, with aviation forecasts predicting substantial growth in air traffic, the industry faces the dual challenge of managing this growth, while adhering to environmental constraints. The air traffic increase, as demonstrated in figures 1.2, is proving to be resilient to external shocks, and even despite the significant shock of Covid-19, the traffic has resumed and is increasing substantially (see Fig. 1.3).

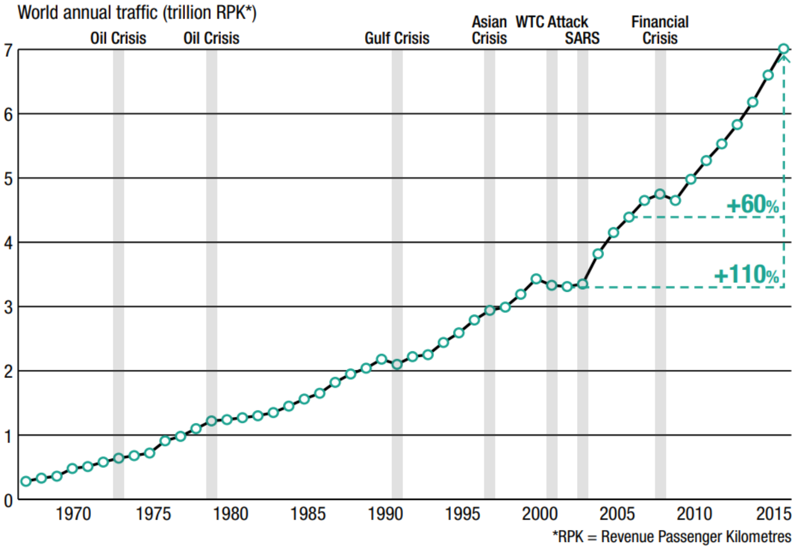

Figure 1.2: Air traffic growth over the years, proving to be resilient to external shocks [7].

As the aviation sector prepares to fulfill the need for more than 41,000 new aircraft over the next two decades [8], balancing operational requirements with environmental constraints is more critical than ever.

In the face of this challenge, governments and airport operators have implemented measures such as noise abatement procedures, noise barriers and soundproofing of homes to reduce the impact of airplane noise on communities [9]. But with urbanization and increasing air traffic, the problem may continue to grow and require more advanced noise reduction technologies, and stringent regulations on noise pollution from airplanes to be put in place. International organizations as ICAO have been working in this direction, setting international standards and goals to reduce aircraft emissions. [10]

In light of this, the aviation sector is actively seeking greener technologies. These efforts are part of broader goals, such as the ACARE 2020 and Europe's "Flightpath 2050" [11], which set ambitious targets for noise reduction, as well as for net CO2 emissions for all intra-EU flights and those departing the EU, to be reduced by 55% compared to the 1990 baseline [11]. Concurrently, the FAA's programs [12] in the United States are focused on developing aircraft technologies that lower both emissions and noise levels.

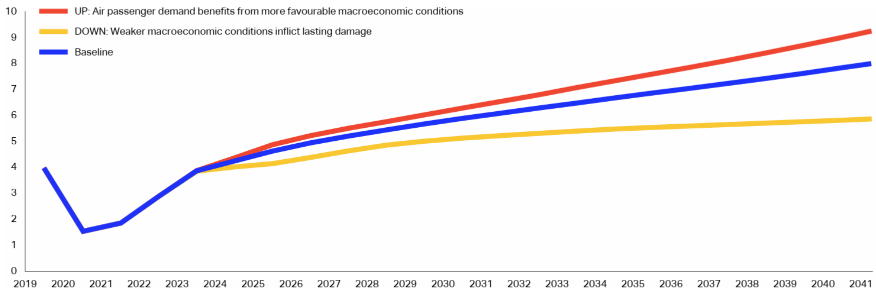

Figure 1.3: Global air passenger journeys, billion [13]

A key aspect of this environmental challenge is the need to reduce both fuel consumption and noise emissions. The development of efficient aircraft configurations and propulsion technologies is not just a response to environmental pressures, but also an opportunity for innovation in aircraft design. Successfully deploying these technologies requires a multidisciplinary approach, combining aerodynamics and aeroacoustics in design optimization processes.

In conclusion, the aviation industry stands at a crossroads, needing to address the growing demands for air travel while minimizing its environmental footprint. This necessitates a holistic approach to aircraft design, one that harmonizes aerodynamic efficiency with low fuel consumption and noise reduction. The successful application of multidisciplinary design optimization (MDO) in this context will be pivotal in shaping an environmentally sustainable and responsible future for aviation.

1.2. Problem Statement

The primary challenge addressed in this thesis is the active reduction of aerodynamic noise in the early stages of aircraft design. Traditionally in the design process, noise reduction has mostly been a secondary consideration, often addressed passively through various mitigation techniques, such as porous trailing edge [14], controlled diffusion airfoils and surface treatments [15]. However, with the aforementioned increasing environmental concerns and stringent regulatory requirements, it is imperative to integrate noise reduction measures directly into the design phase. This proactive approach ensures that aircraft are inherently quieter, rather than relying solely on post-factum noise abatement procedures.

Implementing noise reduction at the design stage involves the use of MDO. This work will be focused on coupling the disciplines of aerodynamics and aeroacoustics, in order to build an optimization framework able to minimize noise, while maximizing aerodynamic performance.

Moreover, the use of a multidisciplinary approach for the optimization poses another problem to be addressed in this research: that is the necessity to keep the computational cost low. High-fidelity simulations, necessary for accurate predictions of aerodynamic performance and noise generation mechanisms, often require substantial computational power and time, making the design process expensive and potentially unfeasible, particularly for more rapid design iterations. Therefore, a crucial aspect of this thesis is to explore and develop methodologies that can reduce the computational cost of the multidisciplinary optimization. This involves investigating efficient simulation techniques, algorithm optimization, and efficient discipline coupling strategies.

To summarize, the main research question to be addressed in this thesis is:

- **How to minimize drag and noise simultaneously?** This involves integrating noise reduction into the airfoil design phase, focusing on achieving aerodynamic shapes that are both efficient in terms of drag reduction and aerodynamic performance, and effective in minimizing aerodynamic noise.

Constructing a framework able to optimize for both disciplines, within a feasible computational time, would mark a significant step forward in developing quieter, environmentally friendly aircraft while maintaining the practicality and affordability of the design process, therefore representing a significant contribution for the future of aircraft design.

1.3. Thesis Outline

The thesis document will be organized as follows:

- Chapter 1: in this chapter, we start by presenting the context and main motivation behind this work. Following this, we define the research question that will drive the next sections of the thesis.
- Chapter 2: presents a comprehensive literature review, focusing on the current state of the art of aerodynamic shape optimization and current trends in noise reduction strategies in the aviation sector. Furthermore, the focus of the review is to examine the state of the art of coupling methods for the aerodynamic and aeroacoustic optimization, alongside with strategies to reduce the computational cost of the optimization. The final part of this chapter presents the research objectives for this work.
- Chapter 3: the theoretical foundations of aerodynamic and aeroacoustic concepts are discussed in this chapter. The chapter covers the fundamental principles of the aerodynamic solvers used in the thesis work, along with the relevant physics of noise generation in aircraft. The aim is to establish a solid theoretical base for the methodologies and optimization techniques explored later in the thesis.
- Chapter 4: the methodologies used in this research are detailed here. The chapter describes the overall framework adopted for the optimization and the integration of aerodynamics and aeroacoustics. This includes the description of the setup of the solvers, the computational tools employed, and the Multidisciplinary Design Optimization strategy.

- Chapter 5: presents the results of the applied methodologies and optimizations. A critical analysis of the effectiveness of the adopted methodology is presented, together with comparisons with relevant literature works.
- Chapter 6: summarizes the key findings of the research, drawing conclusions on the success and limitations of the optimization framework in achieving the intended goals. A reflection on the implications of these findings for future aircraft design is included. Additionally, the chapter offers recommendations for further research and potential areas of improvement in both methodology and application.

2

Literature Review

In the preceding section of this thesis, we have delineated our problem statement: the simultaneous optimization of aerodynamic efficiency and noise reduction in airfoil design. Achieving this necessitates the implementation of a MDO framework that integrates the complexities of both aerodynamics and aeroacoustics. This chapter of the literature review is devoted to decomposing and investigating the various components inherent to this process. The aim is to survey existing literature with a critical eye, thereby identifying the most appropriate methodologies to be adopted in this thesis.

The initial phase of the research centers around the literature pertaining to MDO, with the first step of it being shape parameterization. This involves a review of the methods employed in defining and manipulating the geometric variables of airfoil designs. Following this, attention will be directed towards the structural and algorithmic aspects of the optimization. This entails an examination of the various optimization algorithms and strategies currently in vogue, mentioning their efficacy and applicability in the context of our specific research goals.

Subsequent to the discussion of optimization methods, the literature review will shift focus to the different methods of coupling aerodynamics with aeroacoustics. The intent here is to critically analyze and compare various coupling techniques, determining which among them offers the most effective and efficient means of achieving the dual objectives of low drag and low noise. This analysis will not only consider the theoretical robustness of these methods but also their practical feasibility in terms of implementation.

Finally, a portion of this chapter is dedicated to the issue of computational cost. Given that some of the coupling methods under consideration are inherently resource-intensive, it becomes imperative to address the challenge of minimizing the computational cost associated with the optimization process. This is not merely a technical necessity but also a practical consideration; the optimization process must be feasible and realistic within the constraints of available computational resources. The literature review in this section will explore various strategies and innovations that have been proposed or employed to reduce computational demands, thereby enabling more efficient and feasible optimization processes. This comprehensive review, thus, sets the stage for the selection and application of the most suitable methodologies for the thesis, ensuring that the research is grounded in robust academic precedents. In view of this, the final section of this chapter will outline the objectives for this thesis, and the research gap which this work is aiming to fill.

2.1. Airfoil Geometry Parameterization

Shape parameterization is the first step to perform an Aerodynamic Shape Optimization (ASO), and it represents the way the geometry is handled and deformed by the optimization algorithm. The efficiency of this step is crucial for a successful outcome of ASO, as it determines the fidelity and range of control available for shape deformation. Next to this, with shape parameterization we determine the design variables for the optimization: a successful parameterization will be able to cover a large design space using a relatively low amount of design variables [16].
Shape parameterization methods can be divided into two macro-categories: constructive and deformative. The first type involves methods which are able to represent a shape purely based on a series of

specified parameters [16]. Examples of constructive methods are Class Shape Transformation (CST) [17] and polynomials and splines. On the other hand, deformative parameterizations start from an existing shape, and deform it to create a new shape. These include methods such as Hicks-Henne bump functions, or Free Form Deformation (FFD) [18], which has been extensively used in the latest works on ASO.

A popular and more classical constructive parameterization method for airfoils is PARSEC (Parameterised Sections). This is widely used and involves approximating each surface with a sixth-order polynomial [19]. A notable advantage of this approach is its utilization of actual geometric properties as design variables, as shown in Fig. 2.1, offering a more intuitive way to control the airfoil shape [16].

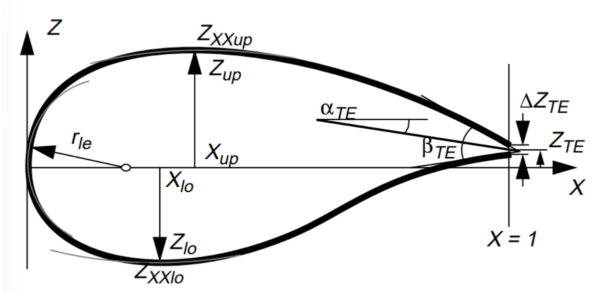

Figure 2.1: Parsec Parameters for an airfoil [20]

Within 2D airfoil optimization problems, various parameterization methods have been tested in literature, and a comprehensive survey is provided by Samareh [21]. B-splines and Bezier curves have been extensively utilized for fitting airfoil shapes through interpolation methods [19]. While effective in reconstructing and optimizing airfoils by manipulating geometry curvatures, these methods encounter challenges in managing the relative positions of control points [22].

Analytical functions have also been developed to represent airfoil families, as documented in the work of Hicks and Henne [23]. Although powerful for representing various airfoil families, this approach may not be suitable for radical new concept designs [22]. In this view, the PARSEC method, utilizing physical airfoil parameters (e.g. leading edge radius, maximum thickness abscissa, trailing edge angle...), proves to be a successful way to define the airfoil shape, using only 11 geometrical parameters (see Table 2.1). Given the geometric understanding of the design variables, and the low number needed to define the shape, which makes it computationally efficient in the optimization problem, PARSEC is considered a suitable parameterization technique to be applied to the case study of this thesis.

Table 2.1: PARSEC Parameters and Definitions [22]

PARSEC parameter	Geometry parameter	Definition
p_1	r_{le}	*Leading edge radius*
p_2	X_{up}	*Upper crest position in horizontal coordinates*
p_3	Z_{up}	*Upper crest position in vertical coordinates*
p_4	$Z_{XX_{up}}$	*Xup upper crest curvature*
p_5	X_{lo}	*Lower crest position in horizontal coordinates*
p_6	Z_{lo}	*Lower crest position in vertical coordinates*
p_7	$Z_{XX_{lo}}$	*Xlo lower crest curvature*
p_8	Z_{te}	*Trailing edge offset in vertical sense*
p_9	ΔZ_{te}	*Trailing edge thickness*
p_{10}	α_{te}	*Trailing edge direction*
p_{11}	β_{te}	*Trailing edge wedge angle*

In Table 2.1, the 11 parameters of PARSEC are described, and they will be used as design variables for the MDO problem.

2.2. Multidisciplinary Design Optimization

ASO is now an essential element in the field of aerodynamic design, given an increasing global demand for new aircraft [24]. Optimization involves finding the most suitable solution to a problem. While some problems may have a single solution, others can have multiple potential solutions. The goal is then to find the “best” solution, or set of solutions, named “optimal”, meaning that no set of significantly superior solutions can be found within the specified framework [25]. A major difficulty in aerodynamic optimization is defining an analysis method capable of running multiple times, and integrating this method effectively with an optimization strategy [24]. These methods need to be both computationally feasible and sophisticated enough to capture the physics of the problem, for a globally optimal system.

The optimization problem can be written as to determine the design variable vector X, such to minimize the objective function J:

$$\min_{X} J(\mathbf{X}) \tag{2.1}$$

with respect to the inequality constraints C_j and equality constraints G_k:

$$C_j(\mathbf{X}) \leq 0, \quad j = 1, \ldots, N_j \tag{2.2}$$

$$G_k(\mathbf{X}) = 0, \quad k = 1, \ldots, N_k \tag{2.3}$$

Within the context of aerodynamic shape optimization of an airfoil, the design variable vector is determined by the parameterization, as explained in the previous section, and eventually flight conditions (e.g. air speed and angle of attack). Each design variable features upper and lower bounds, which represent the range of values the variable can assume. The selection of these bounds is particularly important for an efficient optimization, as it will be explained in 4.1.1. Regarding the constraints, we can distinguish between equality (G_k) and inequality (C_j) constraints. These can typically be of two types: geometric constraints, to limit the deformation capabilities of the airfoil, or constraints related to the objective function (for instance, an aerodynamic constraint of minimum lift coefficient).

Sobieszczanski-Sobieski and Haftka have presented a survey on developments in multidisciplinary optimization for aerospace applications [26].

One of the most relevant advancements in ASO has been the development of gradient-based optimization, coupled with the adjoint method to compute the derivatives, as proposed by Jameson [27]. This approach has proven very effective in optimization problems characterised by high dimensionality of the design space, particularly thanks to the adjoint method, with whom it is possible to compute the derivatives precisely and efficiently, even with a high number of design variables, if the solver is enabled with the adjoint solution [28].

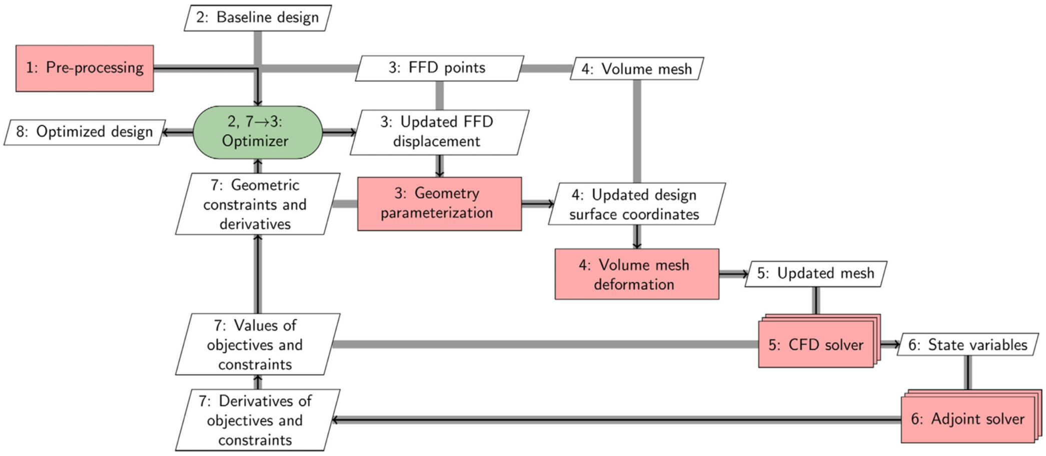

Figure 2.2: XDSM of gradient based aerodynamic shape optimization, MACH-Aero [28]

The Extended Design Structure Matrix (XDSM) of a gradient based ASO can be seen in Figure 2.2, as it is implemented in the open-source software MACH-Aero [28]. As it is clear, the adjoint solver computes the derivatives of the objectives and constraints sequentially after the CFD solver evaluation.

This information is then fed back into the optimizer, which therefore updates the design within the geometric constraints and derivatives. The process of parameterization, deformation and evaluation is iterated until reaching an optimized design. While extensively used in the field of ASO for airfoil optimization [29–31], the adjoint method also presents some limitations, namely:

- **Local Optima**: These methods can more easily get stuck in local minima, and they are highly sensitive to the initial starting point.
- **Dependence on Derivatives**: Gradient-based methods require the calculation of gradients or derivatives of the objective function, which may not be possible for non-differentiable, discontinuous, or highly complex functions. This might represent a problem for this thesis work, as the objective will be to optimize for both low noise and high aerodynamic performance.

Due to the inherent limitations associated with gradient-based methods, this study will explore the efficacy of genetic algorithms (GAs) for the shape optimization of 2D airfoils. Unlike gradient-based techniques, GAs offer a distinct advantage by leveraging population-based search strategies, which can efficiently navigate complex and discontinuous search spaces without the need of calculating the derivatives, and proving higher capability in handling discontinuities during the optimization process [32]. Moreover, GAs inherently possess the ability to explore a diverse range of solutions, thereby mitigating the risk of getting trapped in local minima. This versatility makes GAs a promising alternative for optimizing airfoil shapes to simultaneously achieve low noise levels and high aerodynamic performance.

The optimization through a GA is a method that employs a selective and stochastic search to identify the best possible solution across a vast array of options [33]. Among this type of algorithms, NSGA-II (Non Dominated Sorted Genetic Algorithm) [34] is one of the most popularly used, and it is considered a reference point for comparison of other evolutionary algorithms [35]. In Fig. 2.3, the flowchart of the algorithm is presented. The main steps are:

- **Population Initialization:** The NSGA-II algorithm begins by initializing a population, the size of which depends on the dimensionality of the variables involved. This population can be randomly generated if no prior knowledge is available, with constraints applied if necessary. Alternatively, a more informed selection of initial individuals can be made to potentially accelerate convergence and reduce computational time [36].
- **Nondominated Sorting:** After evaluating the fitness of individuals in each iteration, they are ranked considering both their fitness and crowding distances. Fitness represents an individual's ability to survive and reproduce for subsequent generations, while crowding distance measures how densely an individual is surrounded by its neighbors, calculated as the sum of distances corresponding to each objective. To achieve solutions with appropriate objective function values and good diversity, individuals are ranked based on both objective functions and crowding distance.
- **Genetic Operator:** Using the ranking of individuals, top-ranked individuals are selected as parents for the next generation. Genetic operators are then applied to generate offspring individuals, whose objective functions are subsequently evaluated.
- **Recombination and Selection:** Parents and offspring are combined, and another round of nondominated sorting is performed to assess their fitness. Top-ranked individuals are chosen as parents for the subsequent generation. Individuals are considered nondominant if neither is superior to the other in terms of different objectives. Individuals are ranked so that the first front (Pareto front) constitutes a completely nondominant set, while the second front is dominated only by individuals from the first front. Priority is given to individuals from the first Pareto front. If the desired population size has not been reached, individuals from the second Pareto front are considered until the required number of individuals is satisfied for starting the next iteration.

A more detailed description of the algorithm is provided by Deb et al. [34].

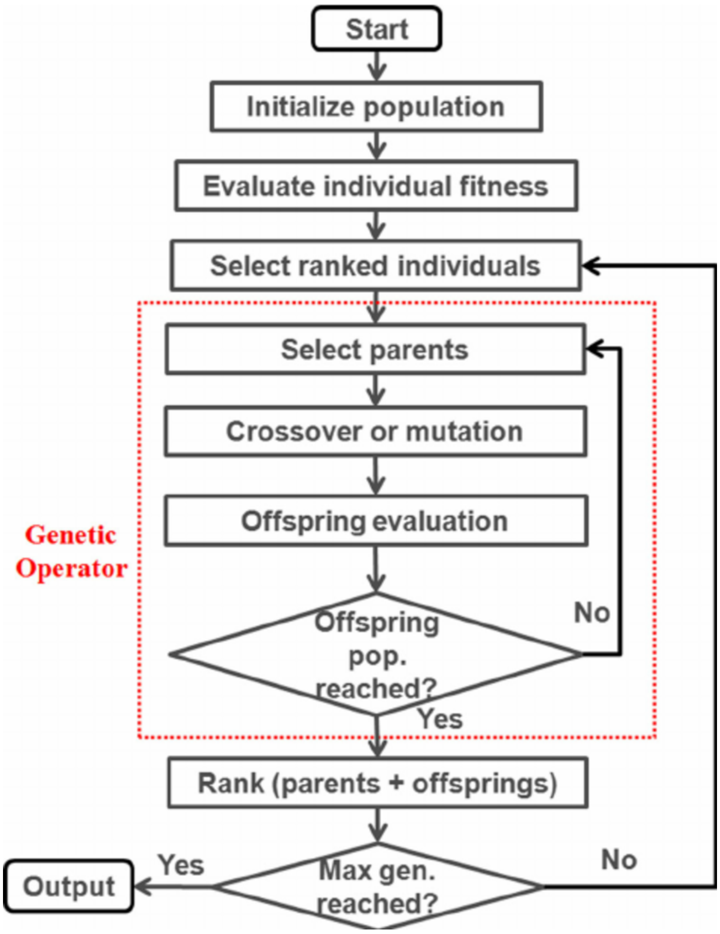

Figure 2.3: NSGA-II algorithm flowchart [36]

For the aforementioned reasons and for its ease of implementation, the NSGA-II algorithm will be chosen to perform the multidisciplinary optimization of this work, which will be illustrated in chapter 4.

2.3. Coupling Methods for Aerodynamics and Aeroacoustics

As previously stated, the research goal of this thesis work is to construct a framework able to minimize both drag and noise. While in principle it is possible to directly compute aerodynamics and aeroacoustics using Computational Fluid Dynamics (CFD) only, this method would result in a too expensive computational cost. This is due to the fact that, if we are interested in computing noise at a far-field location, we would need to extend a fine computational mesh to the entire domain, in order to capture the propagation of small acoustic waves.

In order to avoid this expensive procedure, previous works in literature [37] tackled the problem by sequentially performing an ASO and an Aeroacoustic evaluation. In particular, the ASO framework was run first to obtain airfoils optimized for low drag, after which unsteady simulations were performed for a certain time-span, to obtain the surface pressure distribution on the airfoil at each time step [37]. These aerodynamic data were then processed, and the acoustic signal at a certain position was calculated through the Farassat 1A formulation. Conclusively, the signal has been post-processed, to finally determine the noise levels of the different airfoils to allow for comparison. The flow chart of this process is illustrated in Figure 2.4.

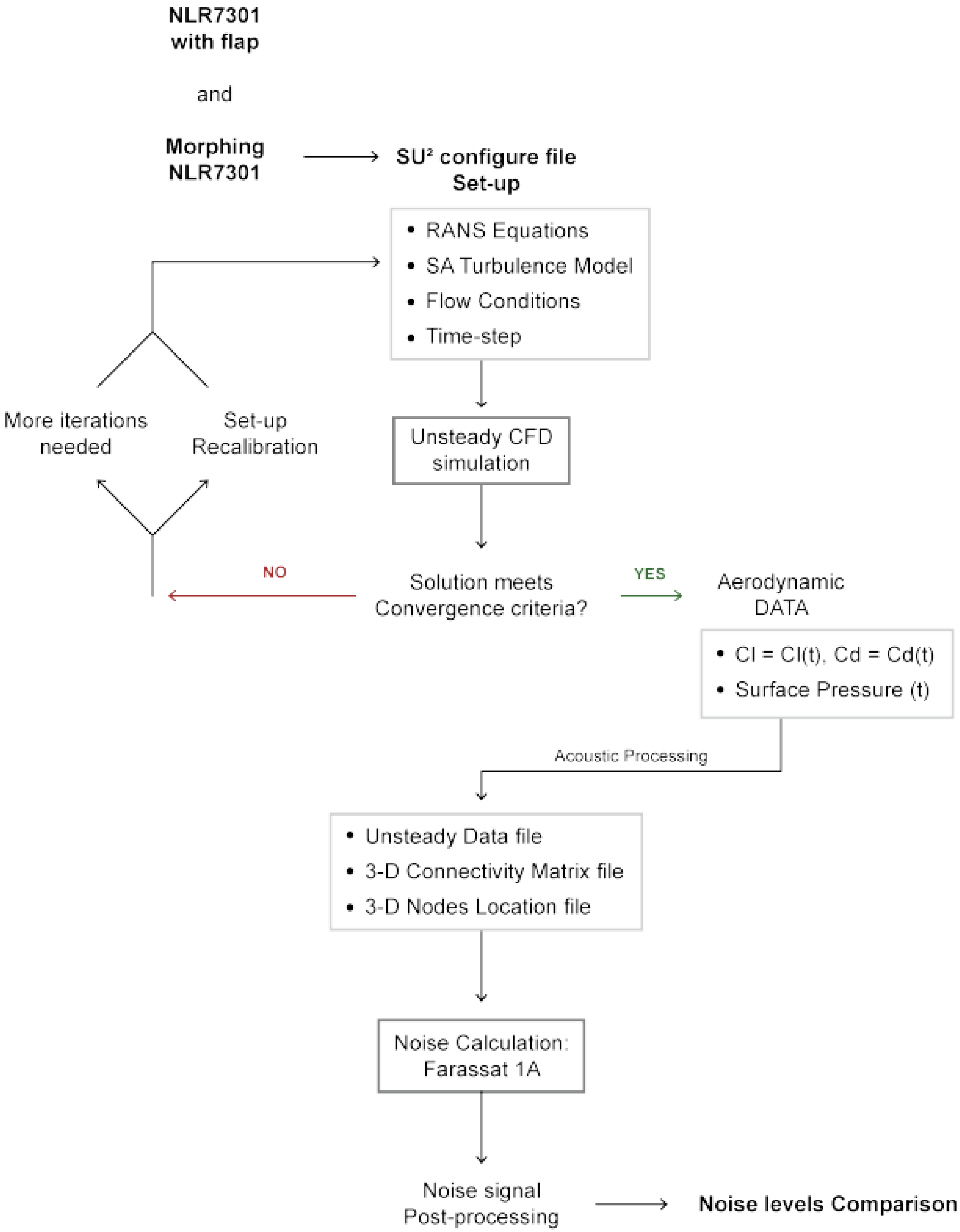

Figure 2.4: Flow chart for the Aeroacoustic framework [37]

While this method certainly does provide a final comparison between noise levels of different optimized airfoils, the aeroacoustic prediction is not implemented within the optimization framework. For this reason, this procedure can be suitable to compare a small number of airfoils of interest, although it cannot be considered as a design tool for optimized aerodynamic and aeroacoustic performance.

In order to improve this and create a tool able to optimize for both disciplines, a coupling method is needed to combine ASO with an aeroacoustic prediction method, so to run the optimization both for low drag and low noise simultaneously. In the next section, an hybrid CFD-CAA approach is introduced as a solution to this problem, along with two different implementations of the aeroacoustic framework.

2.3.1. Hybrid CFD-CAA Approach

A very popular approach to couple CFD and aeroacoustic analysis is to construct an hybrid CFD-CAA framework. The computational domain is divided into two regions ”see Figure 2.5” : a near field region, near the body of interest, where the aerodynamic noise is generated; and a far field region, where the noise is propagated towards an observer.

In this way it is possible to couple a CFD solver with a boundary integral method or finite element method to solve the wave equation in the aeroacoustic domain: a higher fidelity CFD will be used to capture the noise generation process in the near body area, while leaving the propagation of sound waves to a less expensive CAA model [38].

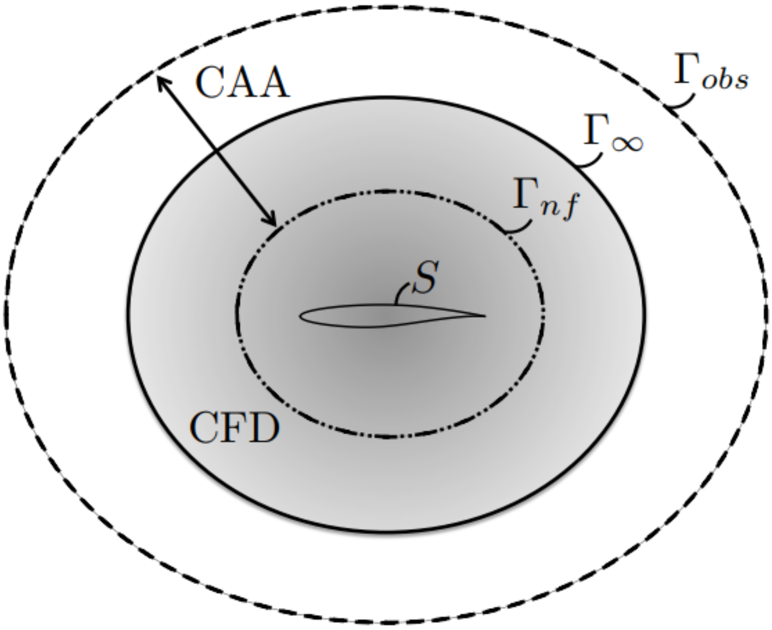

Figure 2.5: Notional schematic of the coupled aerodynamic and aeroacoustic domains. Note that the CFD domain may overlap or be a subset of the CAA domain [38].

In the following subsections, two distinct coupling techniques are presented, both based on the hybrid CFD-CAA framework described. After a brief description of the two methods, it is crucial to assess their efficiency and limitations for specific applications, especially in the context of our thesis work. The feasibility to implement these methods in a multidisciplinary optimization is considered a deciding criterion for the choice of the most suitable framework to use.

2.3.2. Permeable Surface Ffowcs Williams-Hawkings approach

A first attempt to couple CFD and CAA using an hybrid approach is presented by Economon et al. in [39]. In this work, the authors propose a set of continuous adjoint equations for unsteady aerodynamics, along with a continuous adjoint formulation for noise computation [39]. To couple the two disciplines in the hybrid CFD-CAA domain described previously, a new adjoint boundary condition is introduced, relating the local adjoint variables at the interface between CFD and CAA domains [39]. The first step is to define a permeable, fictitious control surface around the body, Γ_{nf}. The shape of this surface is defined by a function, $f = 0$, such that $f < 0$ inside the body and $f > 0$ outside the body [39]. This control surface, as shown in Fig. 2.6, divides the flow domain into two regions, labeled Ω_1 and Ω_2.

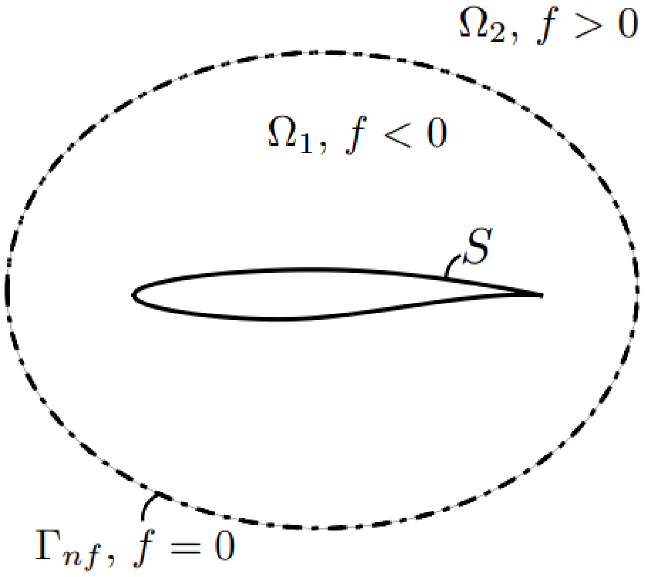

Figure 2.6: Control surface Γ_{nf}, enclosing the physical body surface, S [39]

Once defined this, the focus is to find the sensitivity of the perceived noise at a certain observer location, defined by a surface Γ_{obs} (see Fig. 2.5), due to shape changes on the aerodynamic body of interest, S, which is inside the CFD domain. In order to do this, it is necessary to link the two domains: this connection occurs at the near-field interface, Γ_{nf}, where the CFD solution is used as input for the CAA method, in the form of source terms for the wave equation [39]. In this way, any perturbation to the shape of S will propagate through the CFD solution inside the control surface, and will then be transferred to the CAA wave equation adjoint solver through the source terms at Γ_{nf}. Finally, these will propagate through the wave solution, resulting in a change of total integrated noise at the observer location [39].

While this continuous adjoint approach proposed by Economon et al. [39] seems promising for the coupling of CFD and CAA, the derivation of the interface conditions between the two domains can be problematic. As noted by Zhou et al.[38], deriving the interface conditions is extremely cumbersome for low-Mach number flows, where two separate solvers are necessary to resolve the near-field turbulence and acoustic wave propagation [38]. To overcome this problem, Zhou [38] proposes instead a discrete adjoint approach, which can be eased by the use of Automatic Differentiation (AD). The idea of AD is that any simulation code, regardless of its complexity, is merely a sequence of elementary operations whose differentiation rules are well known [38]. For this reason, it is possible to simultaneously compute both the simulation output and its derivative with respect to prescribed design variables. This technique presents many advantages according to Zhou et al. [38], namely:

- Replacing laborious and error-prone hand differentiation of the discretized equations.
- Leading to robust and consistent adjoints, given that the adjoint solver inherits the same convergence properties as the primal solver.
- AD-based adjoints are by construction, accurate to machine precision, and do not incur in any roundoff or truncation error, like the traditional finite difference methods.

Following the construction of such domain of the problem, the selected method for the wave-equation-based CAA model is an integral method, based on the Ffowcs Williams-Hawkings (FWH) formulation. This offers a efficient approach for calculating acoustic pressure at arbitrary observer locations, by performing boundary integrals once the appropriate field data are known [38]. The governing equation can be written as:

$$\left(\frac{\partial}{\partial t^2} - {a_o}^2 \frac{\partial^2}{\partial x_i \partial x_j}\right)(H(f)\rho') = \frac{\partial}{\partial t}\left[Q_n \delta(f)\right] - \frac{\partial}{\partial x_i}\left[F_i \delta(f)\right] + \frac{\partial^2}{\partial x_i \partial x_j}\left[T_{ij} H(f)\right] \tag{2.4}$$

where

$$Q_n = Q_i \hat{n_i} = [\rho u_i + (\rho_o - \rho) v_i] \hat{n_i} \tag{2.5}$$

$$F_i = L_{ij} \hat{n_i} = [P_{ij} - p_o \delta_{ij} + \rho u_i (u_j - v_j)] \hat{n_i} \tag{2.6}$$

$$T_{ij} = P_{ij} + \rho u_i u_j - {a_o}^2 (\rho - \rho_o) \delta_{ij} \tag{2.7}$$

where the subscript o is for ambient conditions, while the superscript $'$ denotes perturbation values. $H(f)$ is the Heaviside function, which equals 1 outside the control surface, and is zero inside the surface. The acoustic terms on the right side are divided into three parts, namely:

- Q_n is a monopole source, accounting for unsteady mass addition.
- $F_i = L_{ij} n_j$ is a dipole source, given by the unsteady force on the fluid.
- T_{ij} is the Lighthill stress tensor. The double divergence of T_{ij} is a quadrupole term, and takes into account nonlinear effects, such as shocks, vorticity, turbulence, variation in local sound speed, and refraction of waves.

Equation 2.4 is solved using a Green's function method, leading to a boundary integral [38]. Furthermore, Zhou proposes both a 3-dimensional FWH implementation in the time domain using the Farassat formulation, and a 2-dimensional FWH implementation in the frequency domain. Both methods are implemented on SU2 software, which makes the framework appealing for the coupling inside an MDO framework.

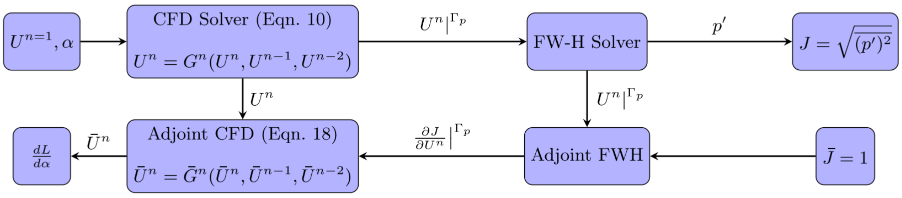

Figure 2.7: Computational chain of the coupled CFD-FWH noise prediction and optimization framework on SU2 [38]

Fig. 2.7 shows the computational chain of the coupled CFD-FWH noise prediction and noise-adjoint framework. At every time step, the flow variables are extracted at each point of the permeable FWH surface, and the monopole and dipole acoustic terms are computed [38]. At the end of the CFD simulation, the respective mean values, which correspond to zero frequency (hence they do not generate noise), are subtracted from the source terms. The pressure fluctuation in time domain can be therefore calculated for each observer location, by numerically integrating along the permeable surface.

As noted by Zhou, this existing Unsteady Reynolds Averaged Navier Stokes (URANS)-based approach primarily addresses tonal noise, proving effective in scenarios where tonal noise dominates due to large-scale fluctuations that URANS can capture. Therefore, to tackle broadband noise, it would be required to explore the utilization of Scale-Resolving Simulations (SRS) such as Delayed Detached Eddy Simulation (DDES) or Large Eddy Simulations (LES), within an adjoint-based aeroacoustic optimization framework. However, applying adjoint methods directly to SRS encounters significant challenges due to the turbulent flow's chaotic nature [38]. Furthermore, in the context of our thesis work, the high computational cost associated with LES simulations makes it unfeasible to be incorporated in the optimization problem. Therefore, we must explore alternative methods for coupling aerodynamics and aeroacoustics to achieve both effective and efficient results.

2.3.3. Parallel coupling interface

In this section, a different approach for a hybrid CFD/CAA method is described. In their recent work, Moratilla-Vega et al. [40] use Aeroacoustic Perturbation Equations (APE) to compute the acoustic propagation, and couple the solver in parallel with the CFD solver, using the open-source library CWIPI.

The advantage of using APE over an integral surface method such as FWH, is that in the APE method the noise sources are determined directly from a flow solution, and the noise prediction is based on the propagation of actual acoustic volume sources, rather than a mathematical projection of the fluctuations as in surface integral methods [41].

The APEs are written in their APE-4 form as:

$$\partial_t p' + \overline{c}^2 \nabla \cdot \left(\overline{\rho} u' + \overline{u} \frac{p'}{\overline{c}^2} \right) = -\overline{c}^2 q_c \tag{2.8}$$

$$\partial_t u' + \nabla \left(\overline{u} \cdot u' \right) + \nabla \left(\frac{p'}{\overline{\rho}} \right) = q_m \tag{2.9}$$

where p', and u' are acoustic pressure and acoustic velocity vectors [40].

The parallel-interface coupling flow-chart for the CFD and CAA solvers is shown in Figure 2.8. The main steps of the coupling process can be described as follows:

- The two solvers are launched in parallel, with CWIPI controlling the communication between the processors.
- Each solver performs the grid partitioning and loads the case set up.
- The coupling is defined by specifying mesh connectivity, variables to be exchanged and type of discretization.
- After this, the CFD solver performs a defined number of time steps before sending relevant acoustic sources data to the CAA solver.
- Acoustic Solver receives the data and computes the wave propagation. The solvers are kept synchronized with a wait function, before continuing to the next step.
- Finally, at the end of the simulation, each solver writes the results and the coupling is terminated.

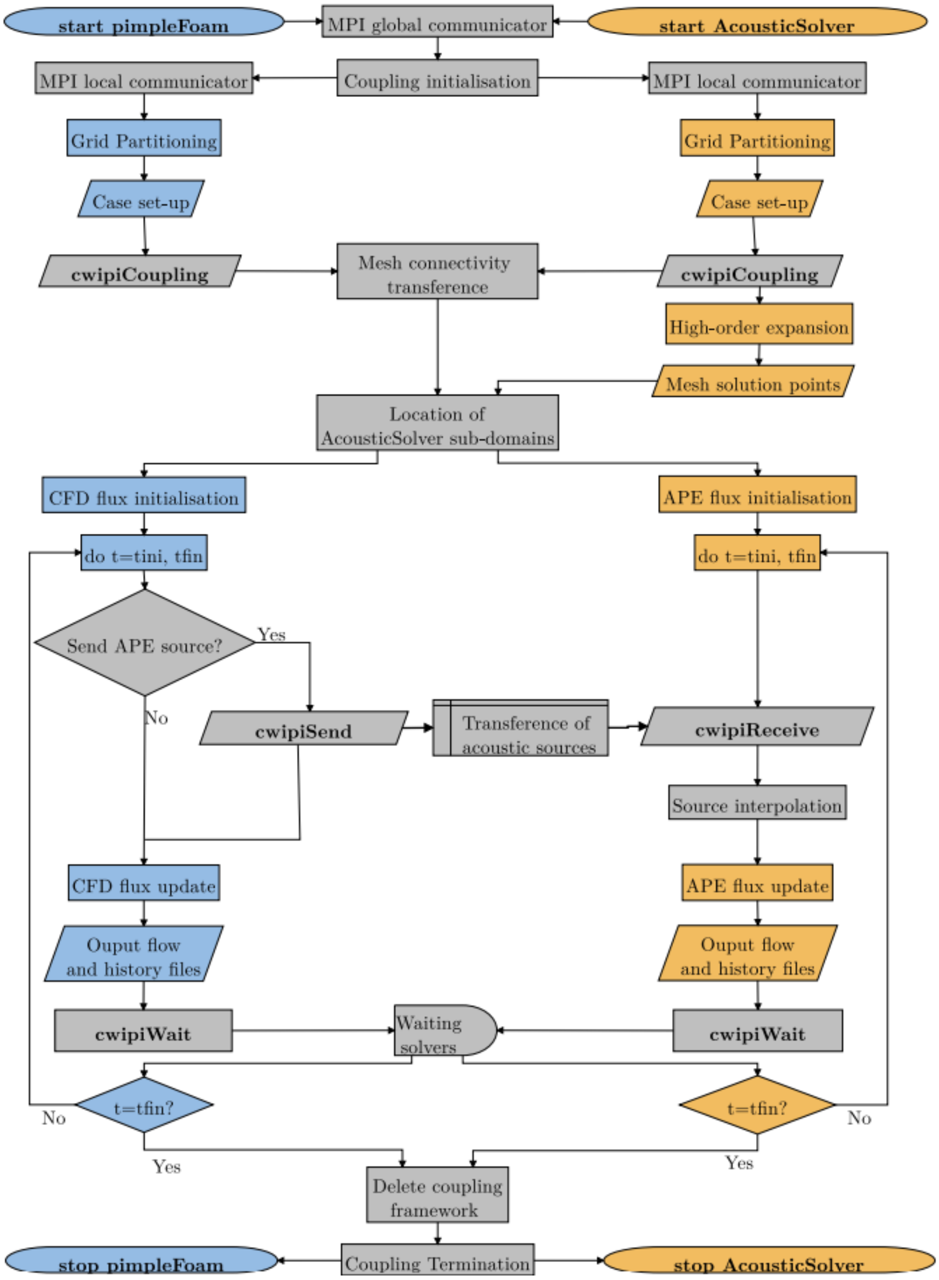

Figure 2.8: Parallel-interface coupling for CFD (blue) and CAA (orange) solvers. The coupling tool is shown in grey. [40]

In conclusion, while the hybrid CFD/CAA method employing APE coupled with the open-source library CWIPI presents a promising approach for characterizing various aeroacoustic problems with considerable flexibility, it may not be the most efficient choice for our thesis work. Despite the advantages of APE, as demonstrated by Moratilla-Vega [40], certain limitations arise, particularly in the context of predicting noise utilizing coarse meshes [40]. As illustrated, the APE method relies on a flow solution to directly determine noise sources, and its noise prediction is based on the propagation of actual acoustic volume sources. However, when coarse meshes are employed, the accuracy of the predictions may be compromised. This limitation poses a concern for our specific thesis work, where the efficient prediction of noise on coarse meshes is crucial. The computational expense associated with the APE method, especially in the context of an MDO loop, could be prohibitively high. Therefore, alternative methods that offer a more computationally efficient solution for our specific application need to be explored.

2.3.4. Trailing Edge Noise

Addressing airframe noise reduction poses a significant challenge, particularly due to the need to meet strict noise emission standards set by regulatory authorities. While reducing noise from undercarriages and high-lift devices is essential, this alone is not enough. For an aircraft approaching the runway to land, when engine noise is less intense due to its low power demanding, airframe noise becomes crucial, and specifically Trailing Edge Noise (TEN) [42]. Trailing-edge noise, a key noise mechanism in this configuration, results from the energy scattering of turbulent eddies in the boundary layer as they pass over the trailing edge.

Simulating and predicting this broadband trailing-edge noise is only part of the challenge. For optimal aircraft design, it's essential to use these simulations to assess aeroacoustic far-field noise, and then iteratively refine the design based on the outcome. In order to compute TEN, it has been proven that the adjoint methods described in the preceding section present some complications, due to the chaotic nature of turbulence [43].

Yet, recent findings indicate that the chaotic nature of turbulence in these simulations leads to challenges in obtaining reliable adjoint solutions, due to regularization issues [43]. Furthermore, the limitations of traditional simulations, such as the URANS, become clear, in their inability to characterize broadband noise. URANS primarily addresses tonal noise, without resolving transient turbulent structures crucial for broadband noise generation [42]. Consequently, optimizations based on URANS may effectively reduce tonal noise but leave broadband noise levels unchanged [44].

Given these issues, and the high computational demands associated with these, it becomes important to investigate a more efficient alternative for assessing broadband noise. In their recent study, Volkmer and Carolus [45] focused on the shape optimization of an airfoil, specifically targeting noise reduction. The methodology they employed utilized several tools and models: XFOIL [46] for turbulent boundary layer parameter prediction, the Kamruzzaman [47] model for wall pressure spectra prediction beneath a turbulent boundary layer, and Amiet's [48] model for far field noise prediction. The optimization aimed at the sole minimization of trailing edge noise, while ensuring a minimum lift requirement. Their approach involved integrating a fast, semi-empirical trailing edge noise model, with a low fidelity aerodynamic tool such to forecast lift, drag, and boundary layer parameters. However, despite an efficient computational cost, Volkmer concluded that the aeroacoustic models used might not sufficiently capture the optimal airfoil shape concerning trailing edge noise [45].

In a more recent study, Ricks et al.[49] aimed to improve Volkmer's work by incorporating a RANS solver, which, compared to XFOIL, would enhance the sensitivity to small airfoil profile changes, leading to a more accurate representation of flow physics and noise generation mechanisms.

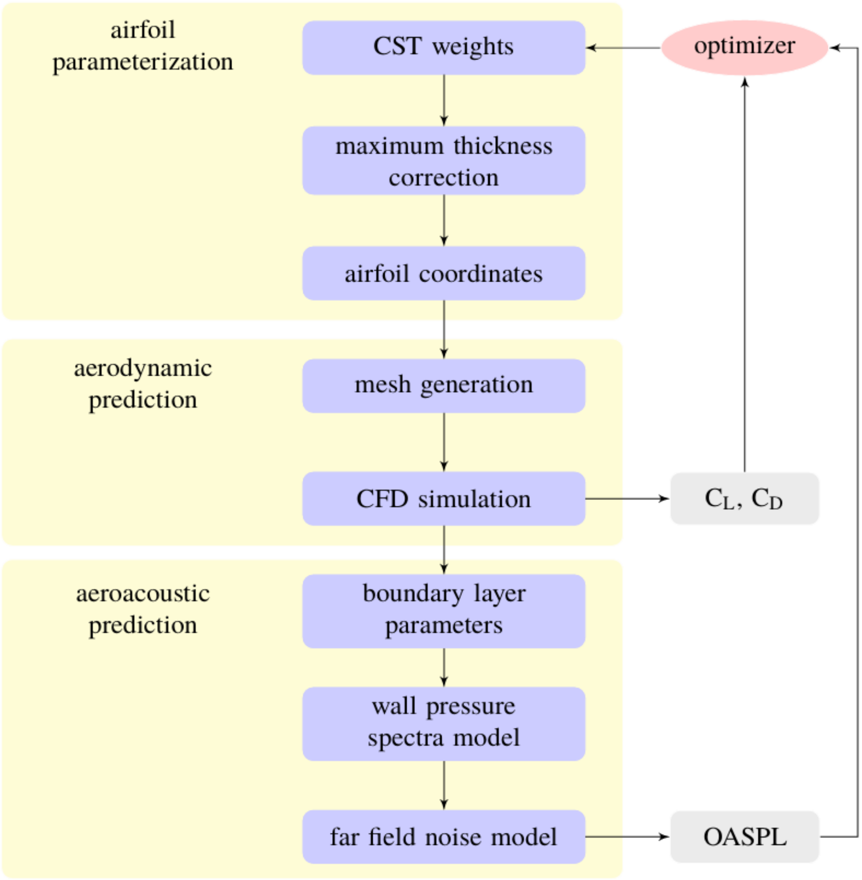

Figure 2.9: Flow chart of the solving strategy of Ricks [49]

Küçükosman et al. [50] demonstrated the superior performance of RANS flow simulations combined with the Lee [51] wall pressure spectra model and Amiet's far field noise prediction model in predicting trailing edge noise. This approach outperformed the Kamruzzaman model used by Volkmer and Carolus [45], and the flowchart of the solver can be visualized in Fig. 2.9. This approach proved to be promising both in terms of results accuracy and in terms of computational efficiency. As advised by Ricks, the inclusion of multiple angles of attack and varying mean flow velocities would be an important step to broaden the scope and comprehensiveness of the study. For these reasons, this solving strategy will be chosen as reference point for the development of this study.

2.4. Methods to reduce Computational Cost

As explained in the previous sections, the research goal of minimizing drag and noise imposes the need of utilizing two solvers: one for aerodynamics, one for aeroacoustics.

Furthermore, when incorporating the solvers into an optimization framework, the computational cost becomes even more critical. The optimization process involves running multiple simulations to search for the optimal solution, which can quickly become infeasible if these are too computationally expensive. Therefore, reducing the computational cost of aerodynamic and aeroacoustic simulations within an optimization framework is essential to make the optimization process more efficient and cost-effective, and represents one of the focus points of this work.

In the last years, there have been significant advancements in methods to reduce the computational cost of simulations. These methods have evolved through several stages, driven by the increasing complexity of simulations and the need for more efficient ways to analyze and optimize systems.

One of the earliest methods to reduce computational cost was the use of reduced-order models (ROMs). ROMs are a type of surrogate model that approximate the behavior of a system using a lower-dimensional representation. These models have been widely used in various applications [52, 53]. The most common ROMs are proper orthogonal decomposition (POD) and balanced truncation.

Later on, Kriging and response surface models (RSMs) emerged as popular non-deterministic surrogate models for reducing computational cost. Kriging is a type of statistical model that can be used to make predictions based on limited data, while RSMs are mathematical models that describe the relationship between input and output variables. A fundamental difference between the two methods is that the first one assumes that data point response is correct, but the functional behaviour is uncertain; on the other hand RSMs assume that functional behaviour is correct, but that the data points response has noise [54].

Another popular way to reduce computational cost is to implement multi-fidelity models (MFMs). MFMs combine multiple levels of complexity and accuracy to represent a system, and have been used in a wide range of applications. The main advantage of MFMs is that they can significantly reduce the computational cost of the simulation while still providing reliable results.

In this regard, adaptive metamodels have emerged as a new approach to reduce computational cost of simulations [55]. These models build on the idea of MFMs but in a more dynamic way, by adjusting the level of complexity of the model depending on the uncertainty of the results. The goal of this approach is to optimize the balance between accuracy and computational cost by using lower-fidelity models in regions of the design space that are less sensitive to the problem, and higher-fidelity models in regions where the uncertainty of the results is higher [55].

Finally in the last decade, machine learning techniques have become increasingly popular for reducing the computational cost of simulations. Within an optimization framework, these techniques can be applied to various parts of the process, such as in the geometric design space (with techniques as modal parameterization or geometric filtering), in the aerodynamic evaluation (flow field modelling), or in the optimization architecture, using for instance Generative Adversarial Networks (GANs) or reinforcement learning techniques [56].

Overall, the last years have seen a steady progress in methods to reduce the computational cost of simulations. These methods have made it possible to perform large-scale optimization and uncertainty quantification in a more efficient and cost-effective manner. In the next sections, the most relevant approaches used in ASO will be briefly presented and critically reviewed in the following order:

- Reduced Order Models
- Surrogate Models
- Machine Learning Techniques
- Multi-Fidelity Models

As it will be explained, these techniques can be combined to further reduce the computational cost of the optimization problem.

2.4.1. Reduced Order Models

Reduced Order Models (ROMs) are low-order models derived from some appropriate projections of a full system's DOFs to a much smaller set that encapsulates most, if not all, of the system's fundamental dynamics [57]. The two main purposes to construct a ROM for a given physics problem can be stated as:

- To provide a quantitative, accurate description of the dynamics of the system at a cheaper computational cost than the original numerical model [57].
- To provide a way to easily and quickly interpret the dynamics of the given system [57].

Therefore, a ROM serves as a simplified representation of a physical process, capturing its essential behaviors with fewer degrees of freedom, thereby potentially reducing computational costs. However, this reduction may come at the expense of accuracy and model robustness [57].

The most popular ROM technique is the POD, which employs an empirical spectral method. In such way, field variables are approximated using expansions involving chosen sets of basis functions [57]. To construct a POD ROM, it is necessary to start with a set of system observations, or samples, which are used in the computation of optimal sets of basis functions, in order to represent system variables [57]. Following this strategy, while an initial investment of computation is needed to compute the samples with a high-order method, a great reduction of computational cost is achieved, with the advantage of the possibility of reusing the ROM within a multidisciplinary environment, over a useful range of system states [57].

Yao et al. [53] developed a ROM for gradient based ASO, using reduced Newton's iterations. With this technique, a reduced Jacobian was evaluated through the use of AD. The results achieved show that the ROM is accurate and suitable for subsonic inverse design and transonic flow drag minimization problems [53].

Salmoiraghi et al. [58] proposed ROMs based on POD to speed-up the full-order simulations and make aerodynamic shape optimization more efficient. As their full-order model is represented by a finite-volume discretization of RANS equations, two different POD-based approaches to construct the reduced basis were tested.

These two methods refer to different ways of finding the POD coefficients of the reduced basis. The first one is Proper Orthogonal Decomposition with Interpolation (PODI), which evaluates the POD coefficients through interpolation of the POD coefficients previously found for the sampling points. Due to the simplicity of this process, it is possible to construct a PODI ROM only in the region of interest of the problem, rather than in the entire computational domain. This makes PODI faster and more efficient both in the construction and evaluation of the ROM [58]. The second method proposed is the Domain-Decomposition POD (DD-POD), which was introduced by Buffoni et al. [59] in 2009. As shown in Fig. 2.10, Domain Decomposition means splitting the computational domain into two regions, and using a different approximation method for each one of them.

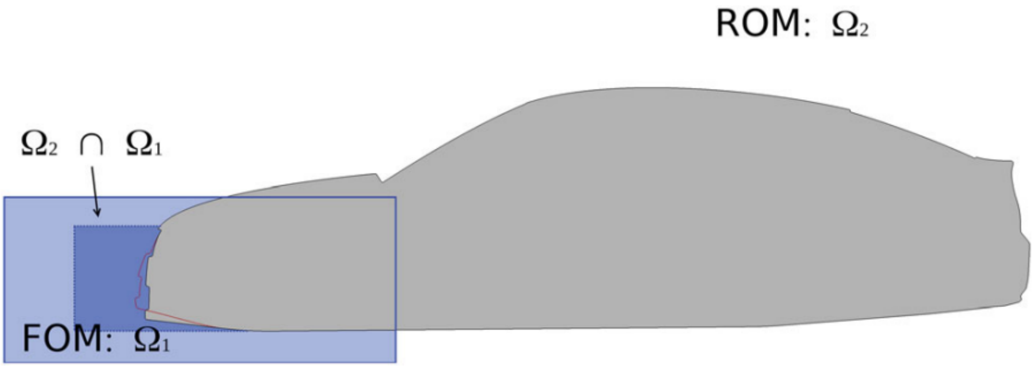

Figure 2.10: Domain Decomposition POD: Ω_1 domain for FOM, Ω_2 domain for ROM, and overlapping region $\Omega_2 \bigcap \Omega_1$ [58]

The rationale behind this method is that POD-based ROMs are usually limited when representing non-linear phenomena, being the POD basis space a linear combination of the solution space spanned by the samples. To overcome this problem, a hybrid approach is adopted, so that a higher order solver is used in the region where non-linearities or geometry variations are predominant, while the ROM is used in the second region. The two regions are then coupled through an overlapping region using a Schwarz-type method. The advantage of this method over PODI is that it makes it possible to reconstruct the whole solution (even non-linear). This feature makes the method more flexible and independent from geometry parameterization. Furthermore, should the field reconstruction be not satisfactory, it is possible to enlarge the high-order domain rather than adding new snapshots, in order to obtain a more accurate result and ultimately requiring less snapshots.

2.4.2. Surrogate Models

Surrogate models are approximations that are fit to the available data and make a functional relationship between input variables and the output quantity of interest. One of the most popular surrogate models is Kriging. Kriging surrogate models estimate the value of a function as the sum of a trend function, usually a low-order polynomial function, representing low-frequency variation, and a systematic departure representing high-frequency variation components [54].

Kriging has become a very popular surrogate model, especially related to multi-fidelity applications.

Fig. 2.11 shows the optimization flowchart presented by Raul and Leifsson [60], using a surrogate model based on Kriging regression, an extension of regular Kriging. In this work, an initial sampling

plan is generated using the Latin Hypercube Sampling (LHS) method. This sampling strategy was first proposed by McKay et al. [61], and it represents an improvement from the random Monte Carlo sampling, being able to provide a good distribution of sample points in the entire design domain.
Following the sampling, a PARSEC parameterization technique is used to generate the airfoil shape, which is then evaluated through a URANS CFD solver. The observations obtained with the evaluation are used to build the surrogate model based on Kriging Regression, and passed on to the optimizer. In case the surrogate model does not meet the termination condition, a new point is added to the initial samples, using an Expected Improvement (EI) infill criterion. By adding new points and evaluating them with the CFD module, it is then possible to iteratively increase the accuracy of the surrogate model, until the accuracy criteria are satisfied. In this context, a very important property of the Kriging based surrogate model is its ability to provide an error estimate at unsampled points [60].

In general, the classical Kriging method is based on the assumption that the objective function is accurate and continuous in the design domain. On the other hand, in engineering problems it is frequent to encounter ”noisy” functions, which include errors in numerical modeling, which might cause issues for the Kriging surrogate model. For this purpose, a Kriging regression SM is used to filter the noisy data, by adding a regression constant to the diagonal terms of the Kriging correlation matrix [60].

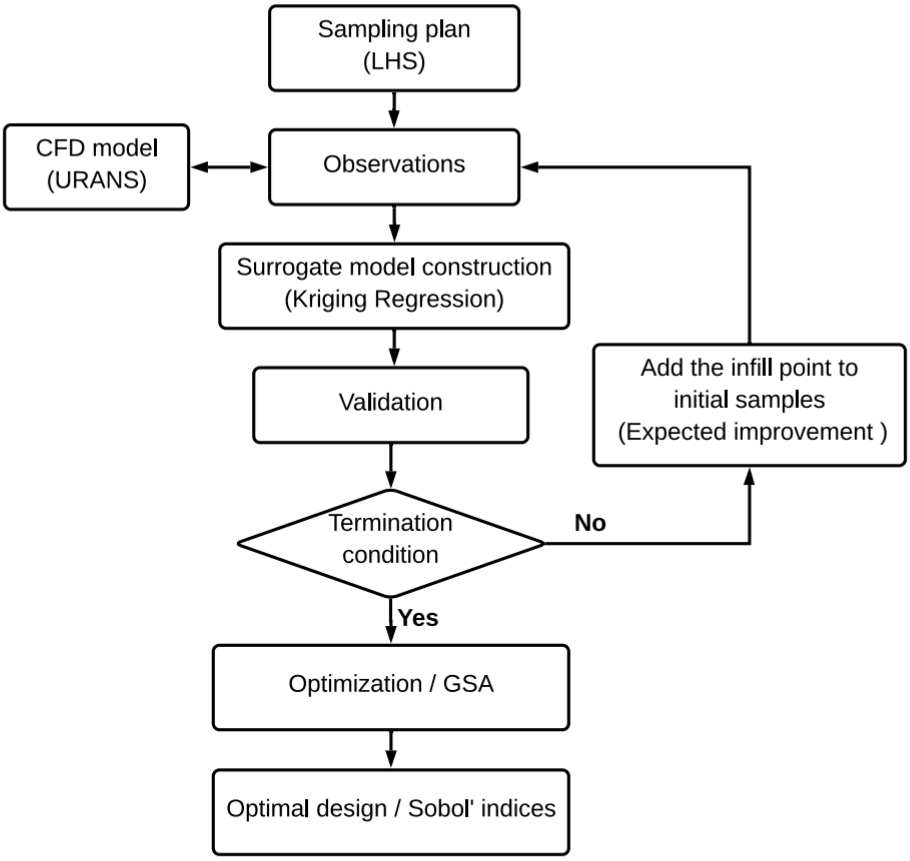

Figure 2.11: Kriging Regression Surrogate-based optimization flowchart [60]

The extension of Kriging, including a multi-fidelity analysis (MFA), is named Co-Kriging, and allows for the construction of an approximation of High-Fidelity Models improved by data from Low-Fidelity Kriging surrogates.

2.4.3. Machine Learning Techniques

Over the past years, Machine Learning (ML) techniques have emerged as a tool to solve physical problems by learning from data [56]. As a matter of fact, trained ML models have extensively proven accurate and reliable results in terms of prediction and description of the underlying physics of the problems they have been used for [56]. The critical and fundamental first step for a ML model to work is to have available data to train the model. In the field of ASO, despite a relatively limited amount of data available, it is possible to generate more data through CFD simulations. The use of ML techniques aims to accelerate this process, through two possible different approaches:

- By constructing data-driven surrogate models to replace the expensive CFD simulations.
- By training neural networks to respect physical laws. These methods are known as PINNs (Physics-Informed Neural Networks).

Overall, the advantages gained by using ML techniques in ASO can be summarized as [56]:

- Reducing the design space dimension, by excluding abnormal aerodynamic shapes and facilitating the convergence of the CFD simulations.
- Taking into consideration aleatory uncertainties in operating conditions and manufacturing inaccuracies, in order to improve the robustness of the model and minimize unexpected performance losses.
- Constructing more flexible metamodels, able to take advantage of experimental data to complement multi-fidelity numerical simulations to guide design optimizations.
- Making interactive design possible by crucially reducing the computational cost of aerodynamic evaluations.

ML techniques can be successfully utilized to address the three most critical aspects of ASO: the dimensionality of the geometric design space, the cost of the aerodynamic analysis, and the convergence rate of the optimization algorithm [56]. A particular focus is put on the geometric design space. In ASO, a precise control of the aerodynamic shape is desired in order to improve the aerodynamic performance. Typical parameterization methods used in ASO, such as CST and FFD, tend to introduce a large number of points, which are then used as design variables, to ensure the inclusion of the optimal design within the design space. The problem with this technique is that these large design spaces often contain abnormal or unfeasible shapes, which might in some cases cause problems to the convergence of the solver. Li et al. [56] introduce two possible ways to cope with this issue and therefore shrink the design space:

- Modal Parameterization: this technique has been frequently used from the 2000s to the 2010s, with the main focus on airfoil shapes, and aims to coupling design variables to shrink the design space.
- Geometric Filtering: this technique has been proposed as an efficient way to exclude abnormal regions of the design space. Unlike the former technique, which reduces the number of design variables, the idea of geometric filtering is to define a constraint function able to evaluate the abnormality of shapes. These constraints are not based on known equations, rather on data-based models.

2.4.4. Multi-fidelity Models

Lastly, a very promising technique to handle the computational cost of an optimization is to build a MFM. A MFM is a type of model that combines multiple levels of complexity and accuracy to represent a system. In the context of reducing the computational cost of high-fidelity simulations, a MFM can be used to approximate the behavior of a system with a lower-fidelity model, while still capturing the key features that determine the system's performance. This can significantly reduce the computational cost of the simulation, and provide useful information about the system along with reliable results.

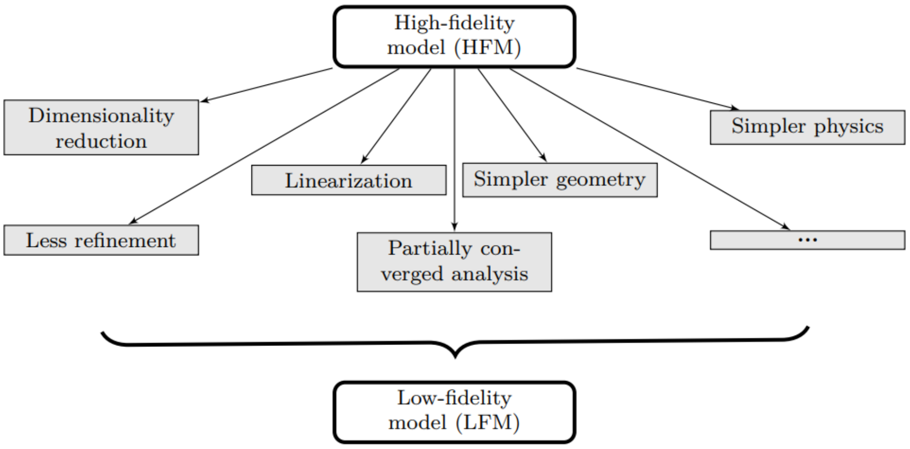

Figure 2.12: Different possibilities to construct a low-fidelity model. [54]

First of all, when referring to a ”low-fidelity” model, we refer to a simplification of a high fidelity model. As depicted in Figure 2.12, there are many different methods to carry this simplification. For CFD based optimization, a common and easy approach to reduce or increase the fidelity of the model is to coarsen or refine the computational mesh, or to use different equations such as potential flow, RANS, LES, or DNS.

Previous works in literature suggest a sequential strategy to combine different fidelities within an optimization. Demiral et al. [62] presented a design optimization study of a missile model, comparing a single fidelity and a multi-fidelity approach. For the single-fidelity case, a Gaussian Process (GP) surrogate model was used. GP is a powerful ML technique, very well known for regression problems [62]. The multi-fidelity method extends the GP from a single function to a set of functions with different fidelities, as a surrogate model [62]. As shown in fig. 2.13, the multi-fidelity approach employs thirty low-fidelity analyses, combined to three high-fidelity analyses. In such manner, it is possible to reduce the use of high-fidelity function evaluations by first evaluating the low-fidelity functions in order to better determine the points which will then be analyzed in high-fidelity.

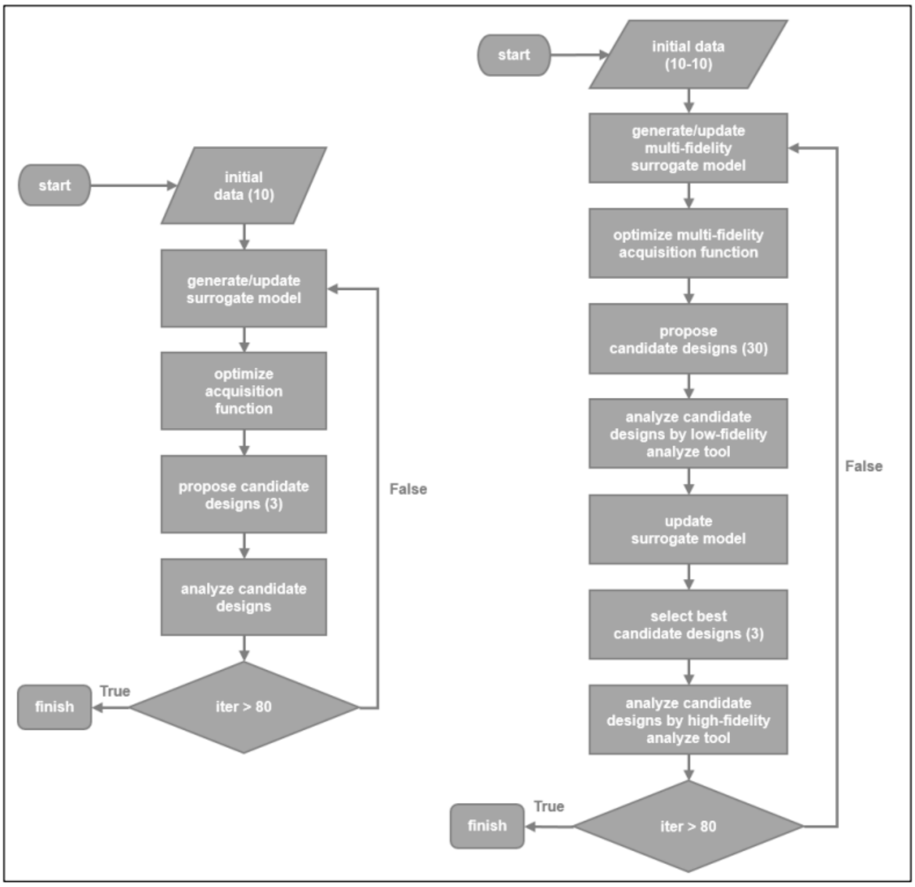

Figure 2.13: Single Fidelity (left) and Multi-Fidelity (right) surrogate based optimization flowcharts [62]

As it possible to see in fig. 2.14, the multi-fidelity method, depicted with solid line in the graph, shows better convergence for both runs (r1 and r2). Furthermore, the study shows that the multi-fidelity results are more consistent compared to the single-fidelity, as the convergence values of the two runs, at iteration 80, are closer to each other. Overall, the conclusion is that the multi-fidelity surrogate-based optimization method significantly accelerates convergence and reduces the computational cost of the optimization, while still attaining reliable results.

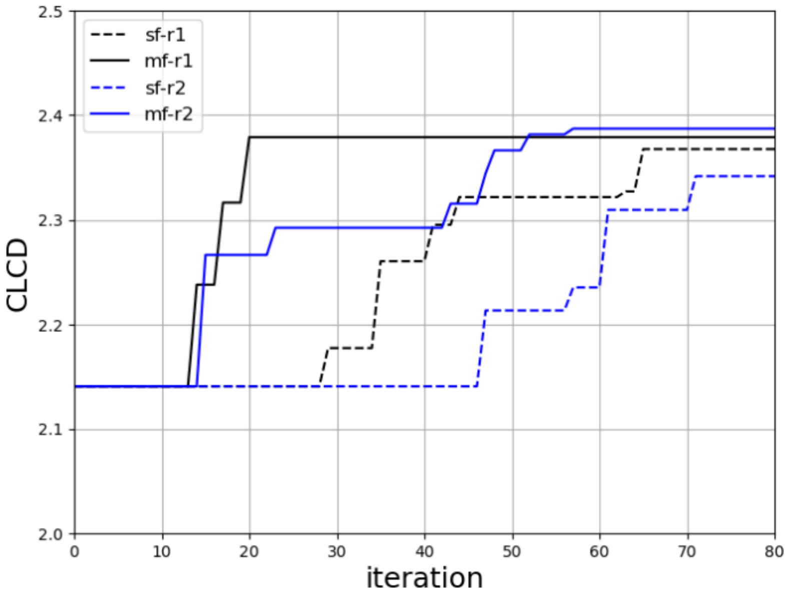

Figure 2.14: Feasible maximum CLCD convergence history for two runs (r1 and r2). Note that ”sf” indicates single fidelity, while ”mf” indicates multi-fidelity [62].

Another interesting application of a multi-fidelity method is provided by Serani et al. [55], in the context of a dynamic metamodel. The performance of surrogate models, or metamodels, is usually problem-dependent, and can be influenced by many different factors, as problem dimensionality, non-linearities, function behaviour or training approach [63]. The idea of developing a dynamic metamodel is to make it function-adaptive, therefore dynamically updating the Design of Experiment (DoE) rather than defining it in the first place. For this purpose, Serani presents a Multi-Fidelity metamodel (Fig. 2.15) which makes use of different fidelities in order to train the model, leading to a further reduction of computational cost of the optimization procedure.

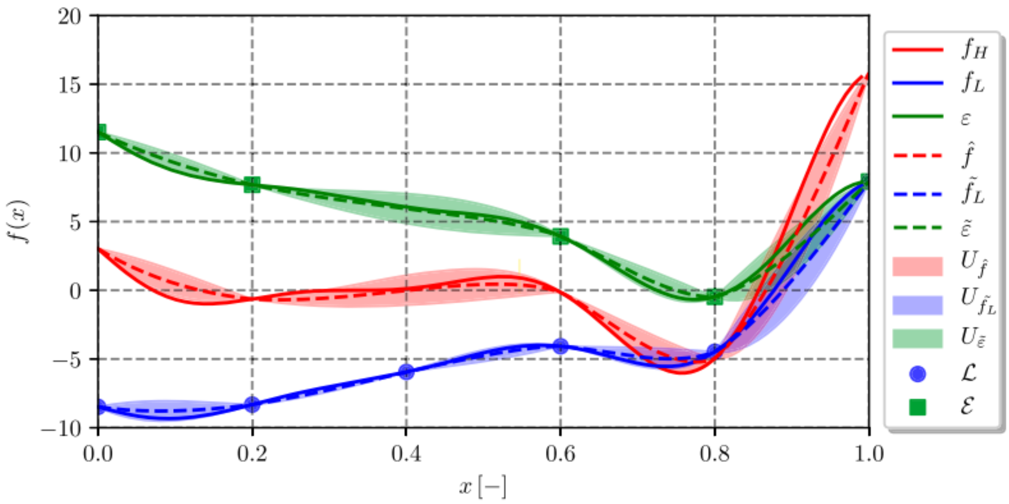

Figure 2.15: Multi Fidelity Metamodel concept and notation. In red, the function is depicted, while in blue is the low fidelity function. In green, the error function. The U indicate the uncertainty associated with each of these functions. Note that ˆ indicates the metamodel prediction, while ˜ indicates the Multi-Fidelity approximation. [55]

In Fig. 2.15, we can see in red the objective function to represent. The blue and green dots are the low fidelity and high fidelity evaluations performed to reproduce the objective function. In this case, an additive correction method was used to correct the low fidelity model, hence:

$$\hat{f}(x) = \tilde{f}_L(x) + \tilde{\varepsilon}(x) \tag{2.10}$$

where the discrepancy $\epsilon(x)$ is the difference between the HF and LF function evaluations. The procedure to dynamically add new training points to the model follows two steps:

- Selection of new training points
- Model refinement through function evaluation

Regarding the selection of new points, Serani et al. [55] proposes different approaches to choose the coordinates of the new training point at each step. One way is the Maximum Uncertainty (MUAS) method, which identifies a new training point simply where the uncertainty of the function is maximum.

$$x^* = argmax[U_{\hat{f}}(x)]. \tag{2.11}$$

With this method, the metamodel will be trained with the goal of minimizing the discrepancy between the model function and the real function, within the entire domain.

A slightly different approach is provided with Aggregate Criteria (ACAS): here, the aim is to find points with both large uncertainty and small objective function value:

$$x^* = argmin[\hat{f}(x) - U_{\hat{f}}(x)]. \tag{2.12}$$

In this way, the focus shifts on the points where the function value is low. This technique can be very promising in the context of an optimization where the objective function needs to be minimized, as it will add training points in the proximity of the global minimum, avoiding useless high-fidelity function evaluations in points where the function value is high (and therefore not interesting in the minimization context). A potential drawback of this method could be relevant in case the function in study presents many local minima: in such case, there is the risk that the method could "get stuck" on a local minimum, thus refining the model in that area and disregarding the rest of the domain.

Once the training point has been selected using one of the mentioned methods, the model is refined based on:

$$\begin{aligned} &\text{If} \quad U_{\tilde{f}_L}(x^*) \geq \beta U_{\tilde{\epsilon}}(x^*), \quad \text{add}\,\{x^*, f_L(x^*)\} \quad \text{to} \quad \mathcal{L} \\ &\text{else,} \quad \text{add}\,\{x^*, f_L(x^*)\} \quad \text{to} \quad \mathcal{L} \quad \text{and} \quad \{x^*, \epsilon(x^*)\} \quad \text{to} \quad \mathcal{E} \end{aligned} \tag{2.13}$$

where $\beta \in [0, 1\}$ is the ratio between the computational cost of the LF and HF evaluation. In this manner, if the inequality is satisfied, meaning that the uncertainty associated with the low fidelity evaluation is high, and the ratio between the computational costs is low, only a low fidelity, cheaper evaluation is performed to refine the model. On the other hand, if the inequality is not satisfied, meaning that the uncertainty of the discrepancy function is high, and β is closer to 1 (hence the computational costs of HF and LF evaluations are comparable), then it will be necessary to run both a high fidelity and low fidelity evaluation on the selected point. The procedure is illustrated in the diagram 2.16. Iterating this method allows for dynamic metamodel refinement at low computational cost, thanks to the presence of the low-fidelity function, and could therefore represent a valid resource in the attempt of running a MDO with unsteady simulations, at feasible computational cost.

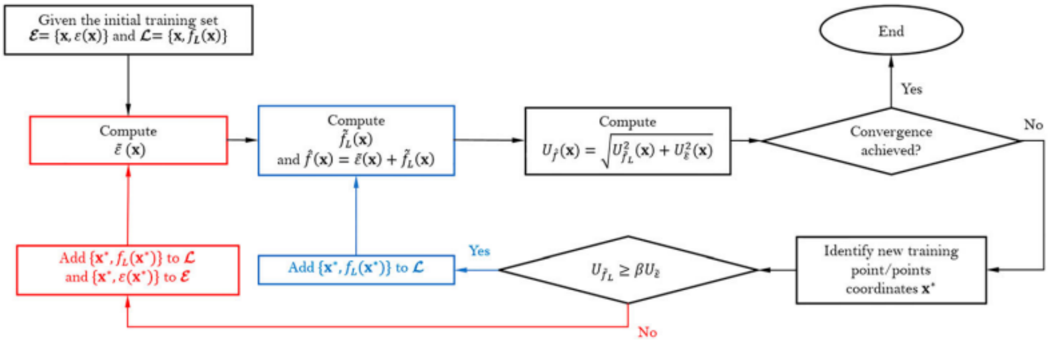

Figure 2.16: Updating scheme for the adaptive multi-fidelity metamodel [55]

This multi-fidelity approach, coupling different fidelity aerodynamic solvers to a Trailing Edge Noise solver for aeroacoustics, and particularly using the adaptive metamodel described, can therefore represent a very promising solution for an accurate and efficient aerodynamic and aeroacoustic optimization framework.

2.5. Summary and Objectives

In the preceding chapters of this thesis, it was presented a comprehensive literature review for addressing the central research question: How can we simultaneously minimize drag and noise in the aerodynamic design of an airfoil? This inquiry is not only critical for enhancing the efficiency and environmental friendliness of airfoils in various engineering applications, but also poses significant challenges, having to consider the optimization of both aerodynamic and aeroacoustic performances. A primary concern that emerged from this investigation is the balance between achieving optimization objectives and maintaining computational feasibility. This final section of the chapter aims to delineate the objectives of this thesis by building upon the insights of the literature review, establishing the next steps to be taken in this work to fill the identified research gap.

1. **Addressing the Dual Challenge of Aerodynamics and Aeroacoustics Optimization**

   As mentioned, the literature survey revealed an additional challenge in the aerodynamic and aeroacoustic optimization: the high computational cost associated with unsteady simulations to predict noise. Such simulations, while providing a detailed understanding of fluid dynamics and sound generation mechanisms, are often impractical for optimization processes due to their extensive time requirements. This highlights the need for optimization techniques that can effectively balance the precision of predictions with computational efficiency, along with the implementation of frameworks to lower the cost of the optimization process. In this sense, among the various methodologies described, MFMs offer a promising path for reducing computational costs, particularly in aerodynamic simulations, considering the spectrum of fidelity levels — from potential codes and XFOIL to RANS or LES — alongside mesh coarsening or refinement techniques, to achieve diverse fidelity levels.

2. **Focus on Trailing Edge Noise**

   Another significant finding from the literature review is the identification of trailing edge noise as a predominant source of noise for airfoils in many engineering applications such as aircraft and wind turbine blades. This insight narrows the focus of our research, allowing us to target specific noise reduction strategies that can have a substantial impact on overall aeroacoustic performance. In this way, we can direct our optimization efforts more effectively, leveraging existing knowledge and methodologies for noise reduction at the airfoil's trailing edge.

3. **Utilizing Fast and Reliable Methods for Noise Prediction**

   Among the various strategies explored in the literature, the optimization of trailing edge noise using the Amiet method stands out due to its speed and reliability. This method, coupled with aerodynamic data obtained from either XFOIL (a lower fidelity solver) or RANS (Reynolds-Averaged Navier-Stokes) simulations (a higher fidelity solver), presents a promising approach for balancing the trade-offs between computational speed and accuracy. Our research aims to build upon these findings, further testing the effectiveness of the Amiet method in different conditions.

4. **Comparative Analysis of Lower and Higher Fidelity Solvers**

   A part of our research objectives is to perform a comparative analysis of the results obtained using lower fidelity solvers, such as XFOIL, against those acquired through higher fidelity RANS CFD simulations. By evaluating the performance and outcomes of these different computational approaches, we aim to identify the most efficient and effective methods for aerodynamic and aeroacoustic optimization. This comparison will not only contribute to the body of knowledge in the field but also guide practical applications in choosing appropriate simulation tools for design optimization.

5. **Multi-point Optimization of 2D Airfoil at Various Flight Conditions**

   Expanding the scope of existing research, this thesis aims to conduct a multi-point optimization of a 2D airfoil under different flight conditions. This involves assessing the airfoil in varying Mach numbers, Reynolds numbers, and angles of attack, within the same optimization. Through this comprehensive analysis, we aspire to develop robust design principles that can be applied across a range of operational scenarios, enhancing the performance and sustainability of airfoil design.

With these objectives, this work aims to add relevant literature in the field of aerodynamics and aeroacoustics optimization, with the ultimate goal to achieve a more efficient and environmentally friendly airfoil design methodology.

3

Theoretical Background

After the identification of the research gap and the research direction we take in this work, this chapter is dedicated to explaining the theoretical background of the methodologies adopted. The fundamental aerodynamic and aeroacoustic principles behind these methodologies will be presented, along with the relevant references in case the reader is interested in getting a deeper insight into these.

3.1. Aerodynamics

In this section, the theoretical foundation of aerodynamic concepts used in this work will be presented. Firstly, an exploration of the significance of aerodynamic coefficients will be conducted, as these coefficients serve as the objective functions to be optimized within the ASO process. Subsequently, the fundamental principles governing the operation of the solver XFOIL will be illustrated. Finally, the rudiments of RANS CFD will be delineated. This comprehensive exposition will lay the base for understanding the subsequent discussions on the aerodynamic optimization methodologies.

3.1.1. Aerodynamic Coefficients

In order to understand the objective functions used in this study, a brief explanation on the typical aerodynamic coefficients is necessary. When an object moves through a fluid medium, it experiences aerodynamic forces arising from the interaction between the object and the fluid. The aerodynamic lift, drag, and moments acting on the object are consequences of pressure and shear stress distributions integrated over the entire body [64]. The lift force, denoted as L, is the component perpendicular to the relative wind direction, while the drag force (D) is the projection along the air velocity direction opposing the body's motion.

The respective coefficients, C_l and C_d, are obtained by non-dimentionalising these forces, making the coefficients independent from variables as the air density, chord, and air speed. This step is crucial to facilitate comparison across different conditions and bodies [65].

Let us first define the dynamic pressure (q_∞) as:

$$q_\infty = \frac{1}{2}\rho_\infty V_\infty^2 \tag{3.1}$$

where ρ_∞ and V_∞ represent density and velocity in the free-stream condition. The lift (C_l) and drag (C_d) coefficients of an airfoil are expressed in terms of dynamic pressure (q_∞) and chord length (c):

$$C_l = \frac{L}{q_\infty c}, \quad C_d = \frac{D}{q_\infty c} \tag{3.2}$$

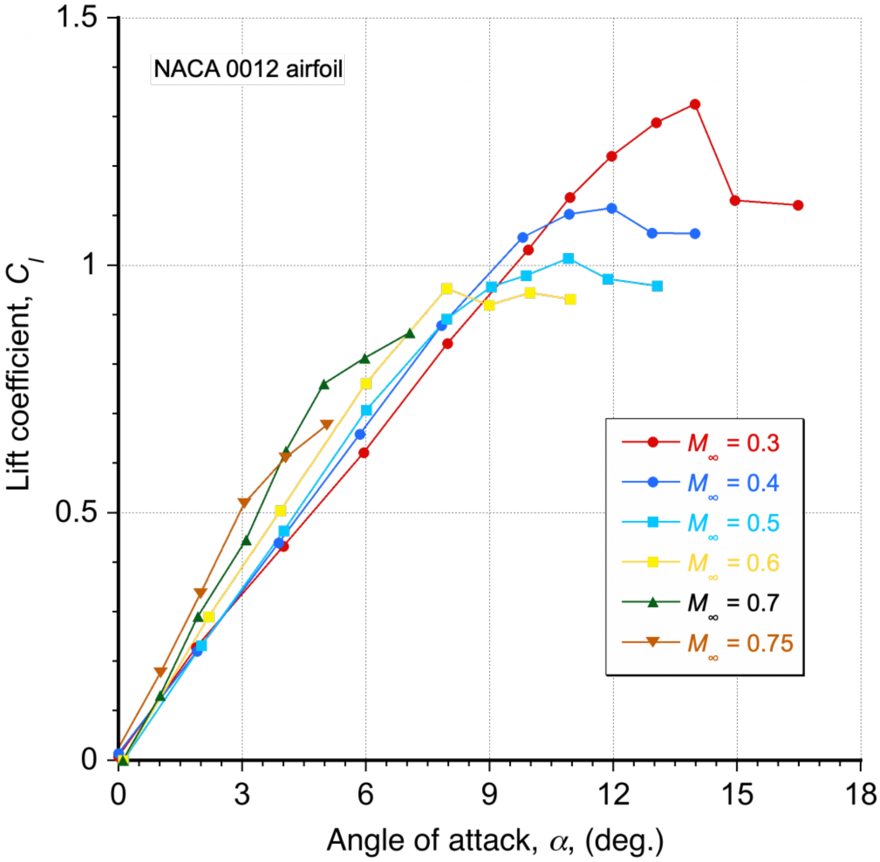

Figure 3.1: Lift coefficient versus angle of attack, at different Mach numbers [66]

In Fig. 3.1, it is possible to see the graph of lift coefficient against angle of attack, or the angle between the airflow and the airfoil chord, for different Mach numbers. This graph, also known as C_l polar, illustrates a fundamental aspect of aerodynamics, crucial for understanding airfoil performance. As α increases, C_l initially increases proportionally. This trend continues until a critical angle of attack is reached, beyond which the airflow over the airfoil separates, leading to the phenomenon of stall. At the point of stall, there is a notable and sudden decrease in C_l due to separation.

Another relevant graph to consider in aerodynamics is the drag polar, which plots C_l against the coefficient of drag (C_d). This graphical representation offers valuable insights into airfoil performance characteristics. For instance, variations in operating conditions such as Reynolds numbers or Mach numbers, as well as differences between airfoil designs, can be easily compared and contrasted on a single plot. Furthermore, an important aspect of the C_l versus C_d graph is its ability to quantify aerodynamic efficiency through the slope of a straight line drawn from the origin (0, 0) to any point on the polar [66]. This slope serves as a measure of the lift-to-drag ratio, with the tangent to the polar indicating the highest slope, and therefore the optimal operating conditions where the airfoil achieves its maximum aerodynamic efficiency. An explanatory drawing is provided by Leishman [66], and shown in Fig. 3.2.

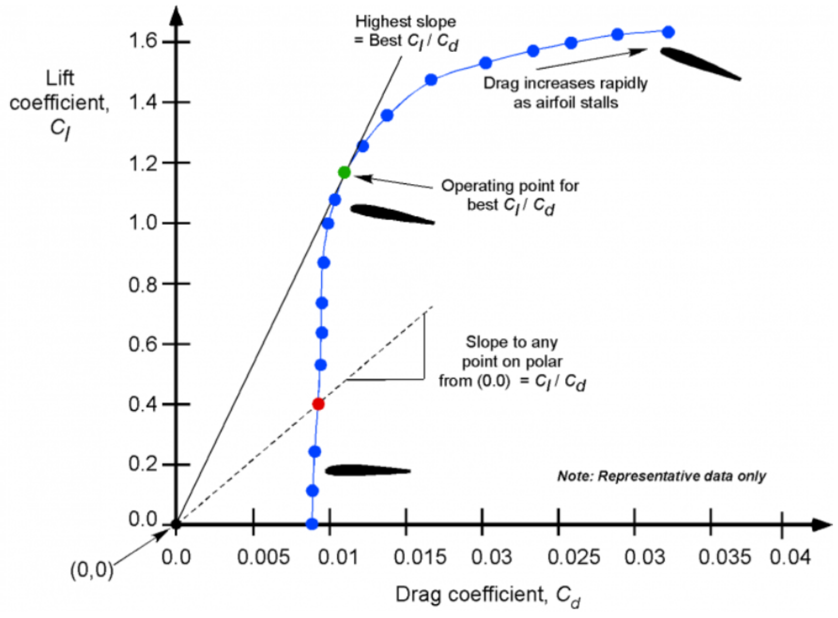

Figure 3.2: Drag polar of a 2D airfoil, as explained in [66]

This basic theoretical knowledge will be necessary to comprehend the setup of the multidisciplinary optimization, and the physical meaning of the objective functions will be defined.

3.1.2. XFOIL

Within aerodynamic analysis, XFOIL stands out as a widely employed and esteemed tool among various aerodynamic solvers. With its versatility and efficacy, it serves as a very promising instrument for a rapid evaluation of the aerodynamic performance of two-dimensional airfoils. Developed by Mark Drela [46] in 1989, XFOIL integrates a potential flow panel method with an integral boundary layer formulation for comprehensive analysis of the airflow around airfoils. This combination allows for a comprehensive examination of airflow around airfoils, particularly tailored for the prediction of airfoil performance at low Reynolds numbers.

The XFOIL code achieves convergence through iterative interactions between the outer and inner flow solutions, focusing on the boundary layer displacement thickness. Noteworthy is XFOIL's ability to calculate viscous pressure distribution, being able to describe phenomena such as trailing edge separation and laminar separation bubbles. Furthermore, XFOIL accurately predicts laminar to turbulent transition locations, a critical aspect in the accurate determination of aerodynamic characteristics. Employing an approximate e^N envelope method [67], the solver tracks the most amplified frequency downstream from a given airfoil point to determine the disturbance amplitude. Transition is triggered when this integrated amplitude reaches a predefined value. The appropriate N value for XFOIL calculations, crucial for this method, is determined by the equation 3.3 proposed by van Ingen [68]:

$$N = -8.43 - 2.4\,\ln(Tu) \tag{3.3}$$

where Tu denotes the absolute turbulence intensity. In this study, N was set to the default value of 9, indicative of a low turbulence intensity freestream.

For the aforementioned reasons, within the context of aerodynamic simulation tools, XFOIL emerges as a prominent choice for researchers seeking an efficient and reliable tool to assess the aerodynamic performance of 2D airfoils, incorporating both potential flow considerations and viscous effects.

Nevertheless, due to its nature of panel code and the assumptions on which it is based, XFOIL presents limitations in accurately capturing complex flow phenomena, particularly at higher Mach numbers. For this reason, it is necessary to implement a higher fidelity solver to be integrated in our multipoint optimization process.

3.1.3. Reynolds Averaged Navier Stokes (RANS)

Given the features and limitations of XFOIL, our objective is to increase the precision of aerodynamic simulations in order to provide a higher fidelity evaluation. Given the goal of keeping computational cost low, DNS or LES are immediately considered impractical within the computational budget. Consequently, RANS emerges as a fitting choice: the application of RANS equations in aerodynamics, and particularly for high-lift configurations and single airfoils, is well-established and widely accepted, as validated by numerous studies [69–71]. Moreover, the use of RANS becomes particularly pertinent at high Reynolds numbers, where the boundary layer transitions into a turbulent regime, necessitating a modeling approach that adequately captures turbulent flow characteristics within the defined computational limitations. This ensures a promising compromise between computational expense and simulation fidelity in the pursuit of accurate aerodynamic analyses. In the following section, it is provided a brief introduction of the RANS equations, which provide a framework for addressing turbulence by considering all unsteadiness as part of turbulence and time-averaging the flow variables.

The idea behind RANS is to execute a time average of the Navier Stokes flow equations. To do so, the Reynolds decomposition is employed, wherein each velocity u component and pressure p are expressed as the sum of their mean values and fluctuating contributions

$$u_i = \bar{u}_i + u_i', \quad p = \bar{p} + p' \tag{3.4}$$

with this decomposition, we distinguish between the mean flow and turbulent fluctuations, allowing a comprehensive representation of the flow [72]. The choice of time averaging is particularly important, ensuring that only turbulence time-scale variations are considered, while other flow features with different time-scales remain unaffected. Failure to adhere to this principle would result in a less accurate flow description.

Subsequently, the equations constituting the entire system are averaged, introducing an unknown term known as the Reynolds-stress tensor. This tensor must be modeled by an appropriate turbulence model to close the RANS system of equations and facilitate its solution.

Consequently, the RANS equations for compressible, viscous flows are presented below, where $\rho\overline{u_i'}u_j'$ is the Reynolds Stress Tensor, which captures the effects of turbulent motions on the mean stresses:

$$\frac{\partial \bar{\rho}}{\partial t} + \frac{\partial}{\partial x_i}(\bar{\rho}\bar{u}_i) = 0 \tag{3.5}$$

$$\frac{\partial}{\partial t}(\bar{\rho}\bar{u}_i) + \frac{\partial}{\partial x_j}(\bar{\rho}\bar{u}_i\bar{u}_j) = -\frac{\partial \bar{p}}{\partial x_i} + \frac{\partial \bar{\tau}_{ij}}{\partial x_j} - \frac{\partial}{\partial x_j}(\bar{\rho}\bar{u}_i'\bar{u}_j') + \bar{\rho}\bar{f}_i \tag{3.6}$$

$$\begin{aligned}\frac{\partial}{\partial t}\left[\bar{\rho}\left(\bar{e} + \frac{1}{2}\bar{u}_i\bar{u}_i\right) + \frac{1}{2}\bar{\rho}\bar{u}_i'\bar{u}_i'\right] + \frac{\partial}{\partial x_j}\left[\bar{\rho}\bar{u}_j\left(h + \frac{1}{2}\bar{u}_i\bar{u}_i\right) + \bar{u}_j\frac{1}{2}\bar{\rho}\bar{u}_i'\bar{u}_i'\right] = \\ \frac{\partial}{\partial x_j}\left[\bar{u}_i\left(\bar{\tau}_{ij} - \bar{\rho}\bar{u}_i'\bar{u}_j'\right) - \bar{q}_j - \bar{\rho}\bar{h}'\bar{u}_j' + \bar{\tau}_{ij}\bar{u}_i - \frac{1}{2}\bar{\rho}\bar{u}_i'\bar{u}_i'\bar{u}_j'\right].\end{aligned} \tag{3.7}$$

Given this, we need to express the Reynolds-stress tensor as a function of mean-field and/or other variables, and this is achieved through turbulence models, such as the Spalart Allmaras (SA) turbulence model [73]:

$$\frac{\partial \overline{v}}{\partial t} + u_j\frac{\partial \overline{v}}{\partial x_j} = c_{b1}(1 - f_{t2})\tilde{S}\overline{v} - \left[c_{\omega 1}f_\omega - \frac{c_{b1}}{\kappa^2}f_{t2}\right]\left(\frac{\overline{v}}{d}\right)^2 + \frac{1}{\sigma}\left[\frac{\partial}{\partial x_j}\left((\nu + \tilde{\nu})\frac{\partial \overline{v}}{\partial x_j}\right)\right] + c_{b2}\frac{\partial \overline{v}}{\partial x_i}\frac{\partial \overline{v}}{\partial x_i}. \tag{3.8}$$

The SA model solves for the undamped turbulent kinematic viscosity, $\tilde{\nu}$. In literature, this turbulence model has proven to give accurate results for many applications, particularly for airfoil and turbine blades. Compared to the low-Reynolds $\kappa - \epsilon$ model, the SA model is considered more robust, reaching convergence and satisfactory results even on relatively coarse meshes [74].

In conclusion, in this work we will consider RANS as high fidelity solver, while XFOIL will be used as low fidelity evaluation. RANS simulations allow for a more comprehensive representation of turbulent flow features and boundary layer interactions, offering a more detailed information about boundary layer separation and transition.

3.2. Aeroacoustics

In aircraft aeroacoustics, trailing edge noise stands out as a prominent noise source, deserving in-detail examination. This section dives into the theoretical knowledge of trailing edge noise, describing the theory and mechanisms of its generation. Its significance lies not only in its perceptible impact on overall noise levels, but also in its implications for aircraft design and operational efficiency. Furthermore, a description of the Amiet approach and assumptions to model trailing edge noise will be provided: this has been widely recognized as robust framework, and will be adopted in this thesis for the aeroacoustic TEN evaluation.

3.2.1. Trailing Edge Noise

Aeroacoustics investigates the generation of noise resulting from aerodynamics. Such noise arises from two primary sources: either from aerodynamic forces acting upon a surface, or from the turbulence within the flow itself, which may or may not interact with nearby surfaces [75].

When flow turbulence interacts with a surface, it induces chaotic pressure fluctuations upon that surface. The abrupt alteration in boundary conditions due to these fluctuations leads to energy dispersion. This phenomenon is notably observed when turbulent boundary layer flow encounters a sharp edge, such as that of a finite flat surface or an airfoil. During this interaction, the conversion of turbulent kinetic energy into acoustic energy takes place, which subsequently propagates to the far field (see Figure 3.3). This form of aerodynamic noise is named turbulent boundary layer trailing-edge noise, or simply TEN. In the context of aircraft aeroacoustics, the noise generated by turbulence at the trailing edge of an airfoil plays a substantial role in the overall sound radiated beneath the flight path. This phenomenon has been extensively studied and documented [76, 77].

The challenge is to formulate predictions in terms of measurable or estimable properties of the unsteady flow over the wing, particularly at flight Mach numbers associated with take-off and landing, typically around 0.3 or lower.

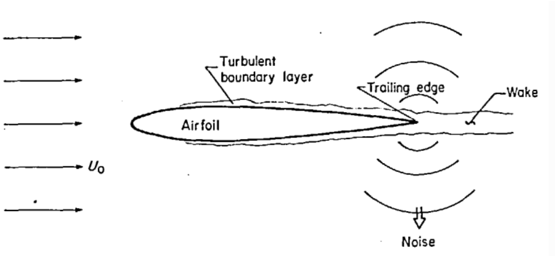

Figure 3.3: Airfoil in uniform flow, generating noise due to the convection of turbulence from its boundary layer past the trailing edge [78].

The examination of trailing edge noise at low Mach numbers was initially undertaken by Powell [79]. Using similarity arguments, Powell estimated the strength of aerodynamic dipole sources located on the plate near the trailing edge. From this model, it was inferred that the trailing edge noise sound power varies approximately as U^4, where U represents the characteristic flow velocity. Additionally, the power spectral density was found to decay inversely as the cube of the frequency at high frequencies [79]. Powell's treatment, however, lacked the necessary detail to predict the field shape of the radiation, and considerations of the effects of flight were omitted from the analysis.

For the prediction of TEN in this study, we can start with the assumption of Lighthill [80], which assumes that in aeroacoustic setting, the surrounding fluid is inviscid and isentropic, therefore:

$$\frac{1}{c^2}\frac{D^2 p}{Dt^2} - \nabla^2 p = \frac{\partial T_{ij}^2}{\partial x_i \partial x_j} \tag{3.9}$$

where T_{ij} is the Lighthill stress tensor, u is the velocity, c is the speed of sound, and ρ is the total density, such that $p = c^2(\rho - \rho_0)$. In this assumption, we consider the Mach number fluctuations small, while the Reynolds number is high, in order to simplify the turbulent source term. Let us now consider the airfoil as semi-infinite flat plate, situated in region $x_1 <= 0$, $x_2 = 0$, and considering x_3 to be an infinite spanwise direction, as shown in Figure 3.4 [75].

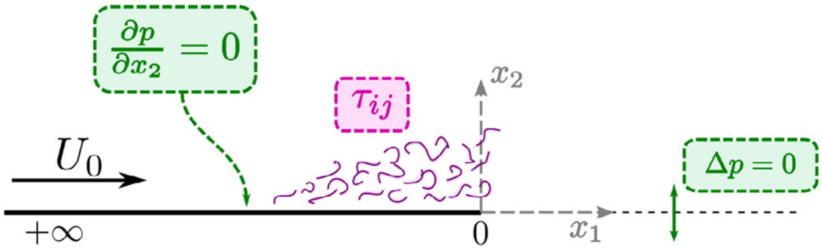

Figure 3.4: Sketch of semi-infinite flat plate assumption, with the corresponding boundary conditions [75].

The challenge is then to solve equation 3.9, and model the Lighthill tensor T_{ij}, under the boundary conditions illustrated in Figure 3.4. To do so, many different models have been proposed in literature: the solution of Ffowcs Williams and Hall [81], and the solution of Howe [82], both based on the use of Green's function; the Wiener-Hopf technique [83], which decomposes turbulence into surface pressure waves of given frequencies; finally the Amiet method [48], which introduces the effect of finite chord length. The aim of the Amiet solution is to obtain a scattered surface pressure distribution on the flat plate, and propagate a finite section of this surface pressure to the far-field. This last approach, due to its popularity in TEN noise minimization works [45, 49], and its ease of implementation, will be used in this thesis.

With reference to the semi-flat plate assumption illustrated in Figure 3.4, Amiet method involves applying a surface pressure at $x_2 = 0$, representing a fundamental surface wave. Additionally, by extending this plate infinitely, Amiet exploits the Schwartzchild solution to obtain the scattered surface pressure distribution on the plate. Subsequently, it extends a finite section of this surface pressure to the far-field using Curle's integral.[75].

The output of the Amiet framework is given by the far field acoustic power spectral density S_{pp}, at a midspan observer x, above the trailing edge at a distance r:

$$S_{pp}(x,\omega) = \left(\frac{\omega r c}{4\pi\sigma_0\delta^2}\right)^2 \frac{2L}{|\mathcal{L}|^2 l_y}\phi_{pp}(\omega) \tag{3.10}$$

where $\mathcal{L}$ is the aeroacoustic transfer function given by Roger and Moreau [84].

For further insights about the Amiet method, the reader is referred to the respective reference [48].

4

Methodology

In this chapter, we treat the methodology adopted to address the research gap identified in the preceding sections. In section 4.1, we offer a clear overview of the entire optimization framework, delineating the tools and techniques employed in our study. Subsequently, in section 4.2 our focus shifts to the low fidelity solver setup, where we elucidate how the XFOIL and Amiet solver were tested and implemented for the purpose of this work. Following this, a description of the high fidelity framework will be presented, detailing all the steps involved in setting up the CFD simulations, which serve as high-fidelity aerodynamic solver. In this regard, we outline the methodology employed to extract the boundary layer parameters from these simulations, which are input to the aeroacoustic Amiet solver. Through this structured approach, we aim to provide a comprehensive understanding of the methodologies used in this study, highlighting the robustness and reliability of our research findings.

4.1. Framework Overview

The primary goal of this research is to develop a comprehensive framework for the multi-objective shape optimization of a 2D airfoil, targeting aerodynamics and aeroacoustics across different flight regimes, specifically during cruise and landing phases. This section outlines the structured approach undertaken to achieve this objective, focusing on the multi-point optimization of aerodynamic performance and TEN.

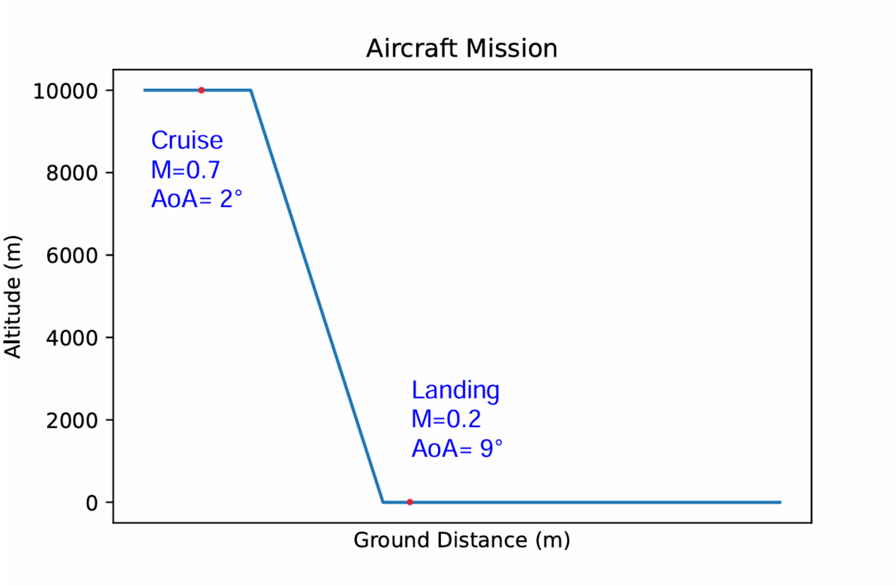

Figure 4.1: Aircraft mission diagram

As a first step, we define the two operational points of the flight envelope which will be considered for the optimization (see Fig. 4.1): at cruise condition, the aircraft is flying at altitude of 10000m, and all the relevant parameters are shown in Table 4.1. At this condition, the objective is to optimize for aerodynamic performance. As will be discussed in the next sections, two different approaches have been tested in the optimization: the first is to minimize C_d at this condition, while the second is to maximize C_l/C_d. The second flight point we will use in the optimization is landing. In this case, it is interesting to evaluate and minimize TEN, as it will be the predominant noise generations source, and the aircraft is in closer proximity to residential areas, thereby having a greater impact on the population's annoyance.

Table 4.1: Comparison of Flight Variables at Cruise and Takeoff Conditions

Variable	Symbol	Unit	Cruise	Landing
Mach Number	M	-	0.7	0.2
Speed of Sound	c_0	m/s	299.67	343.0
Reynolds Number	Re	-	5.95×10^6	4.53×10^6
Angle of Attack	α	°	2	9
Altitude	h	m	10000	0
Density	ρ	kg/m^3	0.4135	1.225
Viscosity	μ	Pa·s	1.46×10^{-5}	1.79×10^{-5}

The optimization framework, as shown in Fig. 4.2, is composed of four main steps:

1. **Parameterization of the Airfoil:** Utilizing the PARSEC parameterization method, nine design variables are transformed into specific airfoil coordinates, serving as the foundation for subsequent simulations.
2. **Aerodynamic Simulation:** The airfoil's aerodynamic performance is evaluated under both cruise and landing conditions using two distinct solvers:
    - *Low Fidelity Solver (XFOIL):* For the low fidelity analysis, XFOIL is used to extract C_l and C_d at both flight conditions. Boundary layer parameters, necessary for aeroacoustic evaluation, are extracted at landing phase.
    - *High Fidelity Solver (RANS Simulations):* Employing the software ADFLOW [85] for high-fidelity analysis, once again extracting C_l and C_d values at landing and cruise, along with the BL parameters at landing.
3. **Aeroacoustic Evaluation:** With the boundary layer parameters derived from aerodynamic simulations, the Amiet TEN model, developed by Zhou with reference to Moreau [84], is employed to compute the airfoil's OASPL, representing the aeroacoustic optimization objective function.
4. **Optimization Algorithm:** The objective functions are then fed into the NSGA-II optimizer. This optimizer then updates the generation of airfoils, until the predefined maximum generation limit is reached. At this point, the last generation of airfoils can be evaluated to analyze the results and check the formation of a Pareto front.

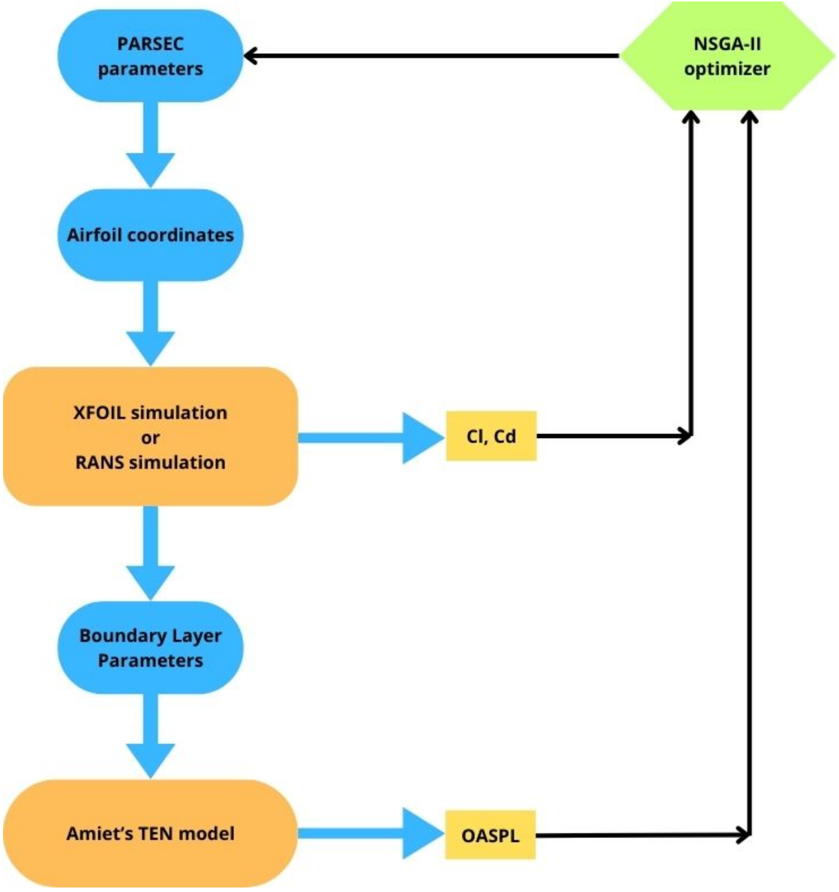

Figure 4.2: Flowchart of the optimization strategy

4.1.1. Optimization Setup

To start the optimization, we first set up the design variables. Based on what we have discussed in the literature review in 2, we are using the PARSEC method to describe the airfoil's shape. As presented in Chapter 2, PARSEC parameterizes the airfoil shape using 11 design variables with physical meaning [20]. In this study, it is decided to keep the TE and LE coordinates fixed at (0,0) and (1,0) respectively, so the chord aligns with the horizontal axis, serving as a reference for varying the AoA, which represents the angle between the free flow and the chord of the airfoil. Due to these reasons, the airfoil shape is in this case parameterized by only 9 variables, which are listed in Table 4.2.

ID	Symbol	Variable name
0	r_{LE}	Leading Edge Radius
1	x_{pre}	Pressure side crest position in horizontal coordinates
2	y_{pre}	Pressure side crest position in vertical coordinates
3	d^2y/dx^2_{pre}	Pressure side crest curvature
4	θ_{pre}	Trailing Edge wedge angle
5	x_{suc}	Suction side crest position in horizontal coordinates
6	y_{suc}	Suction side crest position in vertical coordinates
7	d^2y/dx^2_{suc}	Suction side crest curvature
8	θ_{suc}	Trailing Edge direction angle

Table 4.2: Legend of the 9 design variables used in the optimization

Choosing appropriate bounds for design variables in a shape optimization problem is crucial for ensuring the efficiency and effectiveness of the process. These bounds dictate the range within which the variables can vary during optimization iterations, thus directly influencing the search space explored by the algorithm. Selecting overly restrictive bounds may limit the exploration of potential solutions, potentially leading to suboptimal results. On the other hand, overly broad bounds can increase computational complexity and prolong convergence time [86]. Regarding this matter, the aerodynamic simulation, which serves as the initial crucial phase in the program's workflow, may fail to converge if the airfoil shape is ”unfeasible”, often due to issues with the mesh. Therefore, careful consideration of the bounds for each variable is essential. This typically involves analyzing the physical constraints of the problem, considering the expected range of feasible solutions, and incorporating any relevant domain knowledge or constraints. In this study, many different tests were carried, with different bound selection. For reference, we choose the NACA0012 as a baseline airfoils, whose PARSEC parameters are listed in Table 4.3.

Variable	Value
r_{LE}	0.0155
x_{pre}	0.29663
y_{pre}	-0.06002
d^2y/dx^2_{pre}	0.45150
θ_{pre}	10
x_{suc}	0.29663
y_{suc}	0.06002
d^2y/dx^2_{suc}	-0.45150
θ_{suc}	-10

Table 4.3: Reference Variables for NACA 0012

For each variable, it is decided to have a range of ± 20% from its baseline value of NACA0012.

In the exploration of optimization frameworks, an important decision is the selection of an optimization scheme that adeptly navigates the design space to achieve either maximization or minimization of the specified objective function.

Given the context of this work, where gradients of the objective and constraint functions are not readily available, a gradient-free optimization approach is considered the most suitable. Despite gradient-free schemes being generally more time-expensive and requiring a greater number of iterations to converge, their applicability is justified within scenarios where the design space is relatively constrained and the solver operates with considerable speed. In our work, the 9 PARSEC design variables, with the bound range of ± 20% from the NACA0012 baseline value, along with a computationally cheap aerodynamic and aeroacoustic solvers, ensure that NSGA-II will efficiently perform in the shape optimization of the 2D airfoil.

This algorithm is particularly chosen for its evolutionary nature and population-based methodology, initiating the optimization process with a diverse set of design points. In the case of this work, a Latin Hypercube Sampling (LHS) technique was adopted to generate the initial population for the algorithm.

Furthermore, NSGA-II is engineered for multi-objective optimization problems, where it seeks to optimize multiple conflicting objectives simultaneously. The algorithm does not aim for a singular optimal solution but rather identifies a set of solutions that epitomize the optimal trade-offs between the conflicting objectives, known as the Pareto front. This approach results in a collection of non-dominated solutions, each representing a balance where improvement in one objective necessitates a concession in another. The algorithm's inclusion of elitism strategy and its focus on maintaining diversity in the population highlight its capability to handle the complexities inherent in multi-objective optimization.

For the task at hand, NSGA-II implemented in Pymoo [87]is employed to delineate a set of optimal airfoil shapes across various flight conditions, aiming to maximize aerodynamic performance at cruise and minimizing TEN at landing, while adhering to a lift constraint at landing.

4.2. Low-Fidelity Aerodynamic Solver

In this section, the setup of the low-fidelity aerodynamic solver is discussed. XFOIL serves as a fundamental tool for preliminary aerodynamic assessment owing to its computational efficiency and robustness in predicting airfoil behavior across a range of conditions.

4.2.1. Paneling

Prior to initiating the aerodynamic prediction process, a crucial preprocessing step is executed using the PANE command within XFOIL. This command facilitates the stabilization of the airfoil geometry by rectifying potentially inadequate data points within the associated DAT file. By employing the PANE command, the integrity of the airfoil representation is ensured, laying the groundwork for accurate aerodynamic evaluation.

4.2.2. Computational Parameters

Following the preprocessing phase, the airfoil under investigation undergoes analysis in viscous mode. This mode enables the consideration of viscous effects, essential for capturing the airflow phenomena near the airfoil surface. The analysis is conducted under the relevant conditions of landing and cruise Mach number, Reynolds number, and angle of attack. A maximum iteration limit of 200 iterations is imposed to constrain computational resources while maintaining analytical fidelity. The computational parameters are listed in Table 4.4.

Table 4.4: Simulation Parameters

Parameter	Landing	Cruise
Max Iterations	200	200
Reynolds	4.53 e6	5.95 e6
Mach	0.2	0.7
α (deg)	9	2

With these parameters, XFOIL is able to directly compute the C_l, C_d, C_p, and boundary layer parameters needed as input of the TEN code for the aeroacoustic evaluation.

4.3. High-Fidelity Aerodynamic Solver

In this section, we present the methodology employed for high-fidelity aerodynamic analysis using a RANS solver, specifically ADFLOW [85]. The section includes a comprehensive discussion on various aspects of simulation setup. Firstly, the mesh convergence study, outlining the process of constructing and validating the mesh to ensure its efficacy with the solver. Subsequently, we detail the setup procedure along with relevant parameters utilized in the CFD simulation. To finish, we describe the methodology for extracting the Boundary Layer parameters, which will be used as input of the aeroacoustic code.

4.3.1. Mesh Convergence Study

The mesh convergence study is a crucial step for ensuring that the mesh used in CFD simulations, based on the FVM [88], is both efficient and effective. Spatial discretization of the computational domain into a non-overlapping mesh is fundamental to accurately capture flow physics and obtain meaningful simulation results, as it facilitates the numerical solution of the RANS equations.

The impact of the mesh on simulation outcomes is of great importance, necessitating an analysis of its influence to guarantee the accuracy and reliability of the simulation. Discretization errors, which are inherent in the process of representing continuous governing equations in a discrete form, diminish with mesh refinement, approaching a grid-converged state that matches the continuum solution [88]. However, mesh refinement increases computational demands, highlighting the need for a mesh convergence study to find an optimal balance between accuracy and computational efficiency.

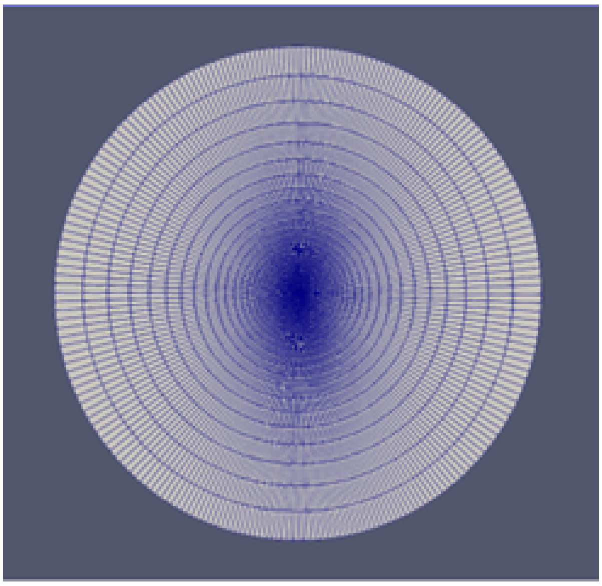

Figure 4.3: O-mesh overview

The aim is to establish a standardized mesh that accurately simulates a variety of airfoil shapes, at the flight conditions of interest, with sufficient accuracy, optimized computational time, and robust convergence properties. To this end, we utilized the pyHyp tool for its hyperbolic volume mesh marching technique, which guarantees mesh orthogonality and precise cell volume control [89]. This method starts with generating a surface mesh for the airfoil geometry, with one cell in the orthogonal direction such as to create a 3D mesh. Following this is the expansion of this mesh into the surrounding volume until a further extension would have negligible impact on simulation outcomes. The use of advanced features in pyHyp, such as spatially variable smoothing coefficients and metric correction, enhances the quality of the generated meshes [89]. With these steps being completed, the mesh is saved and ready to be input of the ADflow solver as a CGNS file. The resulting O-Mesh can be visualized in Fig. 4.3, along with a zoom of the refinement around the airfoil (Fig. 4.4).

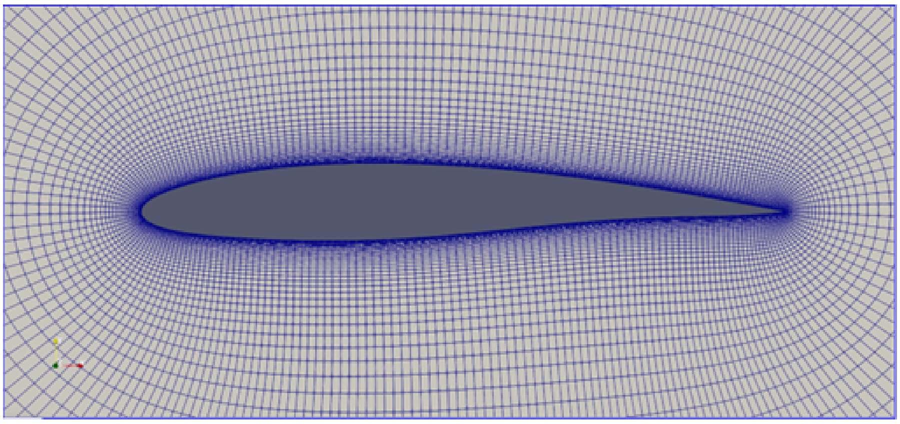

Figure 4.4: Mesh around the airfoil

The key parameters in the meshing process, which can be varied to compare and study the meshing results, include:

- The number of nodes in the off-wall direction, N;
- The thickness of the first off-wall cell layer, $s0$;
- The marching distance between successive layers, d.

The thickness of the first cell layer adjacent to the airfoil surface is critical for capturing viscous flow effects, with the target of maintaining a dimensionless wall distance $y^+ \leq 1$, as recommended for simulations utilizing the SA turbulence model [90]. Selecting the optimal parameters involves balancing wall distance calculations with varying thermodynamic conditions and Mach numbers.

An iterative approach was adopted to fine-tune these parameters, ensuring that changes in the mesh do not significantly alter simulation results, thereby confirming accuracy across both subsonic and transonic conditions. The refinement process within pyHyp begins with the surface mesh, based on provided airfoil coordinates, and extends through the volume mesh, emphasizing the importance of precise initial airfoil curve definition for achieving mesh convergence.

As a first step, a verification is conducted with reference of a NACA0012. For comparison with the experimental results carried out by NASA, we choose to test at $\alpha = 0$, $M = 0.15$, $Re = 6 * 10^6$, and temperature of $T = 300K$. The results of the mesh convergence study can be visualized in Table 4.5 and Figure 4.5. First of all we define the grid ratio as:

$$r_{\textit{effective}} = \left(\frac{N_1}{N_2}\right)^{\frac{1}{D}} \tag{4.1}$$

where N is the number of cells used, and D is the characteristic dimension of the domain. In this study, we decide to refine the mesh at a constant grid ratio of $r = 1.55$. As it is possible to see, with mesh refinement the computational cost increases, and the drag coefficient of the NACA0012 tends to converge. Furthermore, in this phase we can verify the correct functioning of the solver ADFLOW, recognizing that the value for C_d only differs by 0.10 % from the experimental results, and only by 0.06 % from the computation with XFOIL.

Table 4.5: Grid Independence Study for a NACA0012 at $\alpha = 0$, $M = 0.15$, $Re = 6 * 10^6$, $T = 300K$.

N	$s0$	C_d	Δ% NASA	err% XFOIL	t (s)	N cells
83	3.00E-06	8.734	0.09%	0.06%	10	16683
129	2.00E-06	8.49	0.10%	0.06%	20.33	25929
200	1.50E-06	8.48	0.10%	0.06%	153	40200

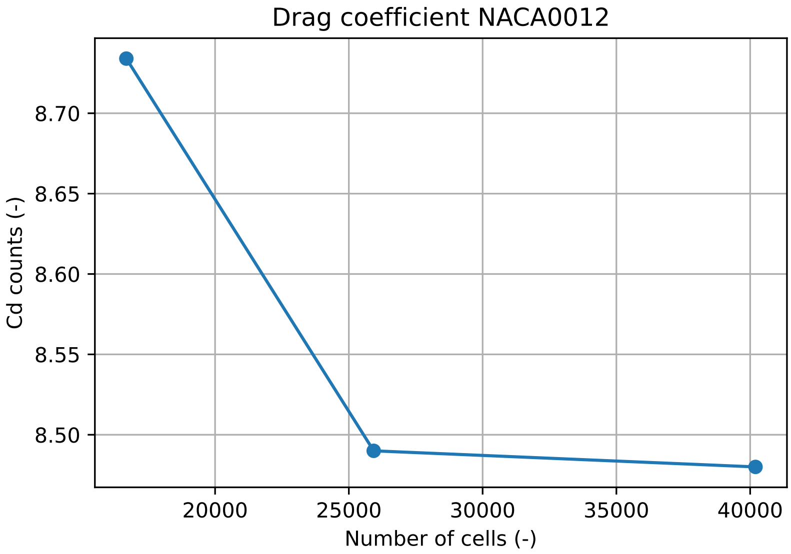

Figure 4.5: Mesh convergence study for the drag coefficient of a NACA0012

As a second step, the mesh convergence study was particularly focused on the cruise and landing phases of the flight mission (see Figure 4.1), whose conditions are defined in Table 4.1. For this purpose, we select an optimized airfoil, result of the low-fidelity optimization, to be the reference for studying the mesh convergence at our cruise and landing conditions.

Table 4.6: Grid Independence Study for an optimized airfoil at landing conditions.

N	$s0$	C_l	C_d	t (s)	Δt	N cells
83	3.00E-06	1.356	0.1630	26	2.07	16683
129	2.00E-06	1.380	0.1593	54	baseline	25929
200	1.50E-06	1.400	0.1590	893	16.53	40200

As evidenced by Table 4.6, there is a robust convergence in the drag coefficient (see Fig. 4.6) when employing consistent refinement with a grid ratio of $r = 1.55$. Similarly, the lift coefficient shows convergence (see Fig. 4.7), with the value approaching $C_l = 1.4$. Overall, this mesh configuration will be adopted for the simulation of the generation of optimized airfoils investigated with the NSGA-II algorithm.

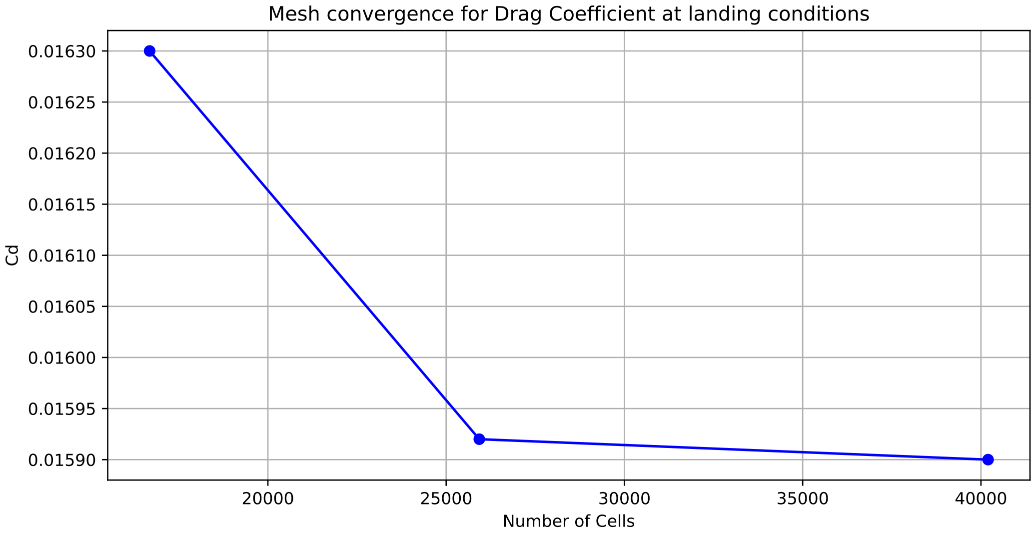

Figure 4.6: Mesh convergence study for the C_d of an airfoil optimized for landing conditions ($M = 0.2$, $\alpha = 9°$).

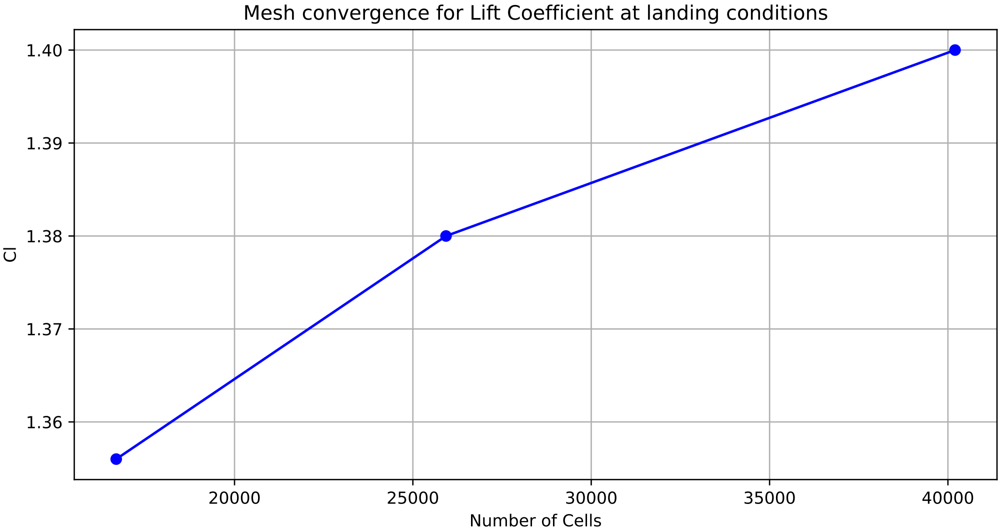

Figure 4.7: Mesh convergence for Lift Coefficient at landing conditions.

4.3.2. Computational Fluid Dynamics Setup

The computational groundwork for the high-fidelity aerodynamic evaluation of the 2D airfoils within this study is based on the utilization of the ADflow software. ADflow is distinguished by its capabilities as a structured multiblock and overset mesh solver that employs finite volume methods, referenced in literature as [85] . Its design allows for the resolution of steady RANS equations. This choice is pivotal, given the objective to accurately represent the physics of airflow across different flight conditions. The SA turbulence model [90], as described in Chapter 3, is selected for its effectiveness in external flow analysis, aligning with the recommendations provided by ADFlow.

Moreover, the software's efficacy is increased by its integration of the Approximate Newton-Krylov (ANK) algorithm [91]. This algorithm serves as a robust globalization scheme of the Newton-Krylov (NK) solver, enhancing the convergence capabilities of the turbulence model selected.

In terms of boundary conditions, the simulations are set to reflect the physical constraints of the problem. Aerofoil surfaces are modeled under no-slip conditions to simulate the interaction with the surrounding fluid accurately. The extremity of the mesh, or the far-field boundary, is configured to correspond with the free-stream flow direction, a process automatically set by the ADflow solver. Additionally, cells with unattached edges are assigned symmetrical conditions to maintain physical consistency. A noteworthy requirement by ADflow for conducting simulations, is the implementation of a three-dimensional (3D) mesh, necessary to setup the solver, regardless of the 2D shape of the airfoil in study. To meet this requirement, it is necessary to establish of a symmetry boundary condition along the artificially created ”span-wise” direction, ensuring the simulation remains representative of the intended 2D aerofoil behavior.

4.3.3. Aeroacoustic parameters extraction

Following the RANS evaluation of the airfoils, it is necessary to extract the relevant boundary layer parameters that are critical inputs for the Trailing Edge Noise code. This process allows for the computation of the Sound Pressure Level (SPL) of the airfoil, utilizing the high-fidelity data obtained from Computational Fluid Dynamics (CFD) simulations. The specific boundary layer parameters required are detailed in Table 4.7.

Name	**Symbol**	**Unit**
Frequency	f	Hz
Convection Coefficient	C	-
Speed of Sound	c0	m/s
Freestream Density	ρ_0	kg/m^3
Freestream Mach Number	M_∞	-
Chord of Section	c	m
Span Section	s	m
Observer Location Coordinates	[x, y, z]	
Boundary Layer Properties		
External Velocity	Ue	m/s
99% or 99.5% Thickness	δ_{xx}	m
Displacement Thickness	$\delta*$	m
Momentum Thickness	θ	m
Wall Shear Stress	τ	Pa
Maximum Normal Shear Stress	τ_{max}	Pa
Chordwise Pressure Gradient	$\frac{dp}{dx}$	Pa/m
Momentum Thickness Reynolds Number	Re$_\theta$	-

Table 4.7: Input Parameters for the TEN Code

The extraction of these parameters from the CFD simulation is facilitated through the use of the Python interface `pvpython`.

To determine the boundary layer thickness, `pvpython` is employed to extract the flow velocity profile in a direction normal to the airfoil surface. As illustrated in Figure 4.8, the velocity profile relative to the normal coordinate is plotted. The boundary layer thickness, denoted as δ, is then defined as the distance at which the flow velocity reaches 99% of the freestream velocity. The small steps that can be observed in the velocity profile are given by the discretization.

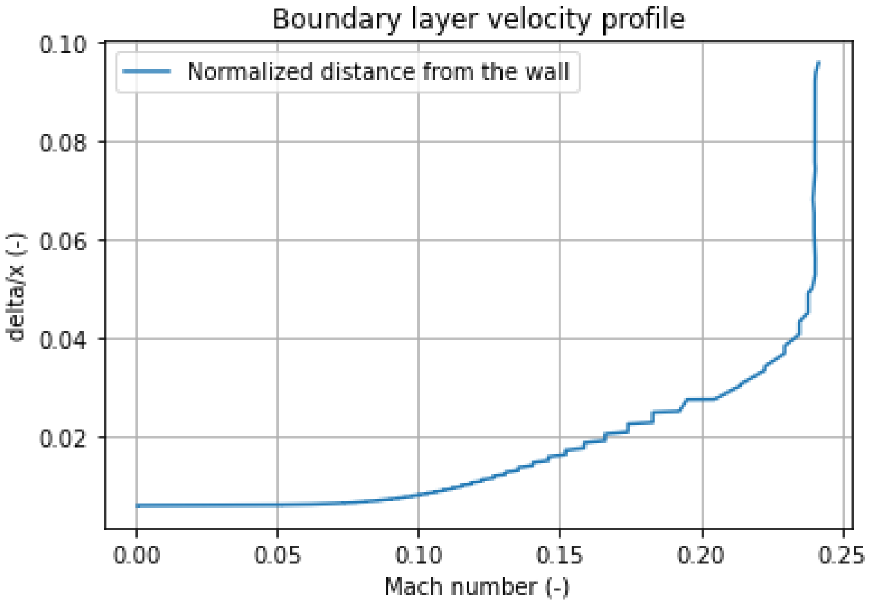

Figure 4.8: Plot of the boundary layer velocity profile. The boundary layer thickness is considered the δ at which the velocity reaches 99% of the freestream velocity.

4.4. Aeroacoustic Solver

In this thesis, we implement an aeroacoustic prediction model for the estimation of TEN generated by airfoils, developed by Zhou, with reference to the work of Moreau [84]. This method primarily relies on the wall pressure spectrum model, which, despite the typically required unsteady flow simulations for noise analysis, allows for estimating the acoustic signature of airfoil TEN using only the flow boundary layer characteristics and surface pressures.

The TEN code computes the Power Spectral Density (PSD), in SPL/Hz, of the TEN generated by a constant section lifting surface with a finite chord and span. The inputs for this model are derived from the aerodynamic flow solutions, and can be visualized in Table 4.7. These BL parameters are extracted next to the trailing edge, particularly at $x/c = 0.97$, as recommended by Rozenberg [92].

The initial phase of this study involves validating the aeroacoustic prediction code by simulating a NACA0012 airfoil. This validation step is crucial to ensure that our computational methods reliably reproduce established results. As outlined in Figure 4.9, the simulation employs our extracted boundary layer parameters to replicate the findings documented by Brooks and Hodgson [78], particularly for frequencies above 1000Hz. The correspondence of our results with these experimental findings confirms the accuracy of our computational model in capturing TEN.

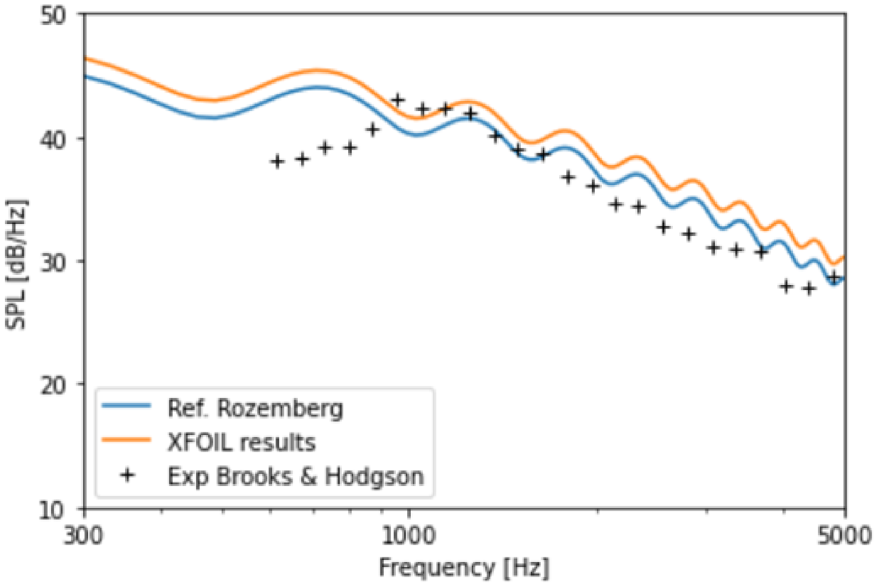

Figure 4.9: Verification of Amiet code

In addition, for the purpose of the optimization, we will utilize the Overall Sound Pressure Level (OASPL) as the objective function. This measure will be computed by averaging the SPL between 1000Hz and 5000Hz. Concentrating on this frequency range not only enhances the reliability of the code but also aligns the study more closely with practical aeroacoustic assessments.

5

Results

In this chapter, we present and critically discuss the results of the optimization processes outlined in Chapter 4. Through a detailed examination, we will present the outcomes of the two distinct optimization approaches we employed, highlighting their capabilities and limitations. Additionally, this chapter will showcase the high fidelity evaluation results, obtained with the use of RANS CFD simulations. A comparative analysis will highlight the significant differences between high fidelity evaluations and the lower fidelity evaluation with XFOIL, underscoring the advantages and disadvantages inherent in each approach. Through this rigorous analysis, we aim to provide a comprehensive understanding of the optimization processes and their impact on the overall objectives, setting the stage for further discussion on implications and future recommendations.

5.1. OASPL and Drag Coefficient minimization

The results of the optimization process of minimizing C_d and OASPL are visualized using Pareto fronts, which effectively illustrate the trade-off between the conflicting objectives of drag and noise reduction. Pareto fronts are a set of non-dominated solutions, considered to be optimal in a multi-objective optimization context. A solution is said to dominate another if it is at least as good in all objectives and better in at least one objective [93]. The Pareto front represents the frontier of such optimal solutions, illustrating the trade-offs between the two objectives. In the case of the first optimization ran in the study, the results yielded very promising and well-defined Pareto fronts, as shown in Fig. 5.1, indicating a successful exploration of the design space and a robust set of optimal airfoil designs under the given criteria.

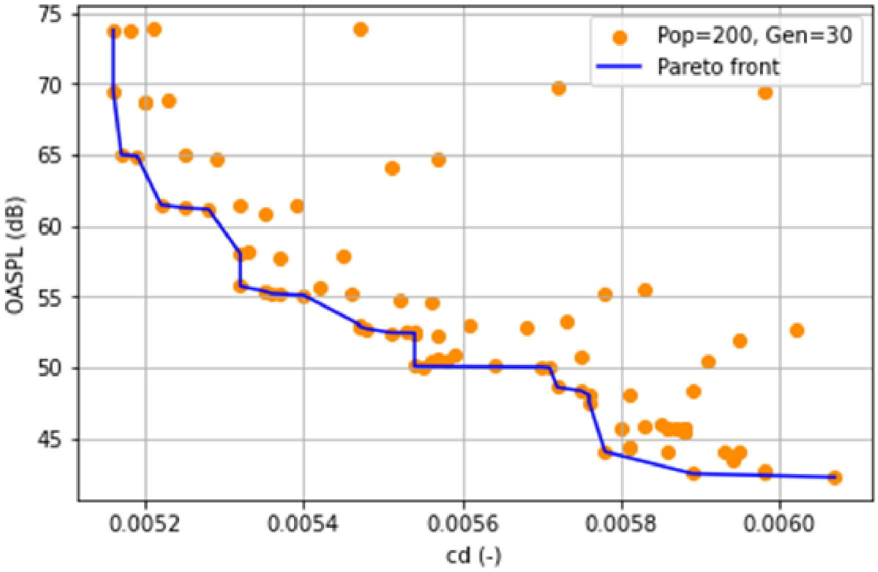

Figure 5.1: Pareto Front for the optimization of C_d and OASPL

Further investigation into the optimization process was to the impact of population size on the definition and quality of the Pareto fronts. Increasing the population size within the NSGA-II algorithm generally led to more refined Pareto fronts (see Fig. 5.2). This is attributed to the larger population providing a broader genetic base, enhancing the algorithm's ability to explore and exploit the design space. Consequently, a higher population size tends to yield better overall results, as it facilitates the discovery of more diverse and potentially optimal solutions.

However, despite the advantages of a larger population size, the analysis of Fig. 5.2 also unveiled that some airfoil designs situated on the Pareto front with a lower population number exhibited superior performance compared to those derived from a larger population. This observation highlights the stochastic nature of the NSGA-II population formation, where the randomness in crossover and mutation can lead to the emergence of performing solutions, even with smaller population size. In this scenario, an optimization using a population size of 200 is considered more efficient than its counterpart with a population size of 400, being able to achieve satisfactory results while also conserving computational resources. On this matter, the optimization ran with population size 200 achieved the results in 332 minutes with 2 processors being used, while the respective optimization with double the population size employed 502 minutes, or 51.2% longer.

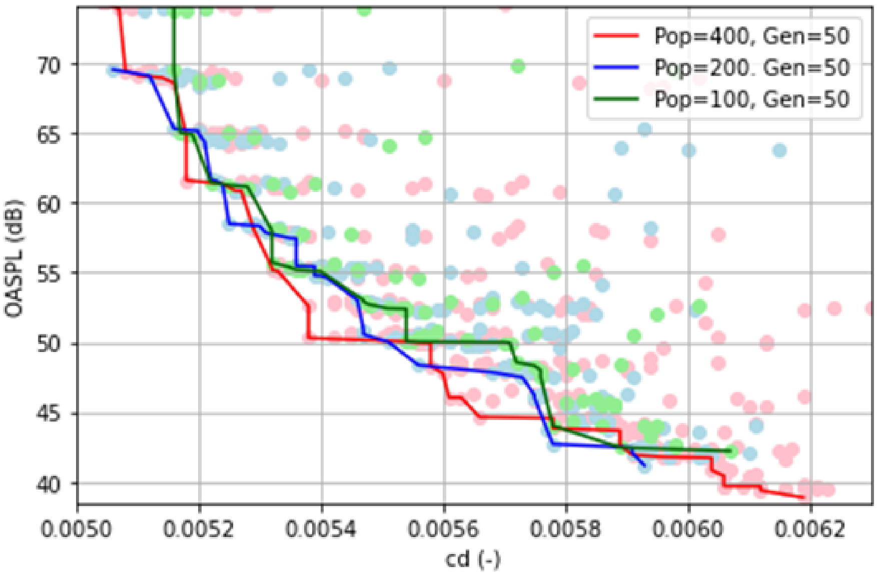

Figure 5.2: Pareto fronts with varying population number

The results of the optimization particularly evident in the comparative analysis of optimum airfoil shapes. Figures illustrating the optimum configurations for the lowest C_d (Fig. 5.3) and lowest OASPL (Fig. 5.4) highlight a notably symmetric profile, with the airfoil optimized for reduced noise prominently featuring an exceptionally thin TE.

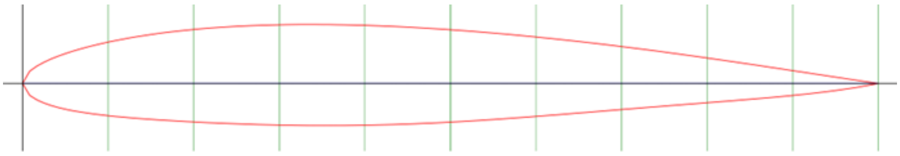

Figure 5.3: Airfoil shape for minimum drag coefficient.

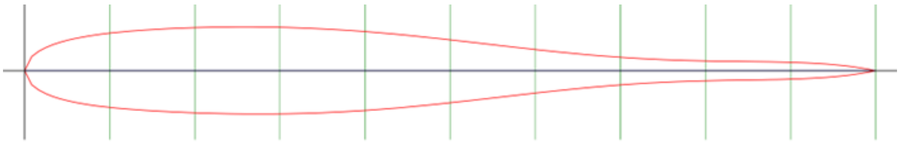

Figure 5.4: Airfoil shape for minimum OASPL.

This characteristic aligns with expectations, given that OASPL is derived from TEN, and the critical parameters for its computation are inherently extracted on the TE. Moreover, an examination of the design variables in relation to their optimized states unveils a recurrent pattern where these variables consistently approach their respective bounds (see Fig. 5.5, either hitting the upper or lower bound). This tendency persists despite efforts to extend these bounds, suggesting an intrinsic drive towards ever thinner trailing edges within the optimization process. Such observations necessitate a reevaluation of the optimization strategy employed. It becomes evident that to investigate more practically feasible airfoil designs, there is the need to change our optimization methodologies, ensuring a more complete and meaningful exploration of the design space.

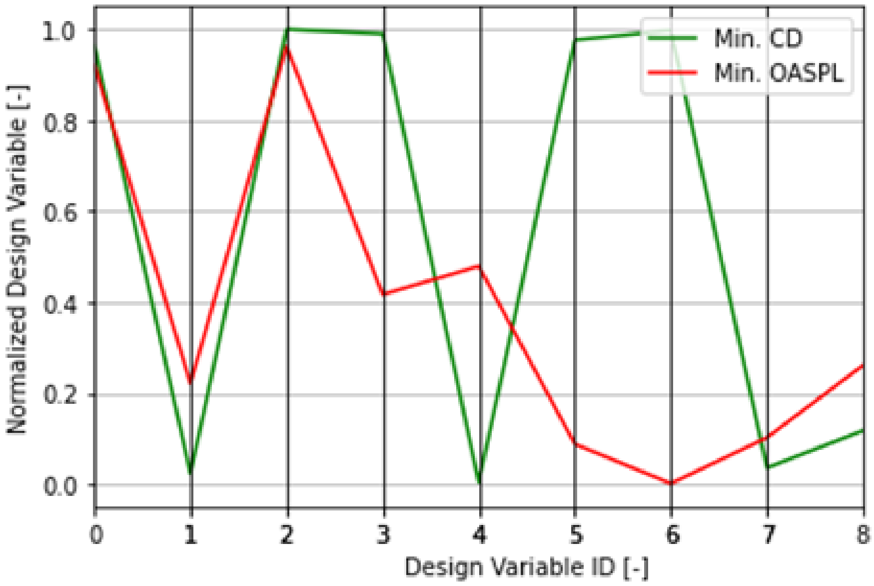

Figure 5.5: Normalized design variables value at optimized conditions

For these reasons, in the next section the focus will be to change the objective functions in order to test a different optimization approach.

5.2. OASPL minimization and Lift-to-Drag Ratio maximization

In the second phase of our optimization strategy, our objective extends to still minimizing the OASPL during the landing phase, while concurrently maximizing the C_l/C_d in cruise flight conditions. An examination of the Pareto fronts, as depicted in Fig. 5.1, highlights again promising results and a well defined Pareto front. This is particularly evident when increasing the population size to 200, which leads to a noticeable increase in both definition and performance (see Fig. 5.7).

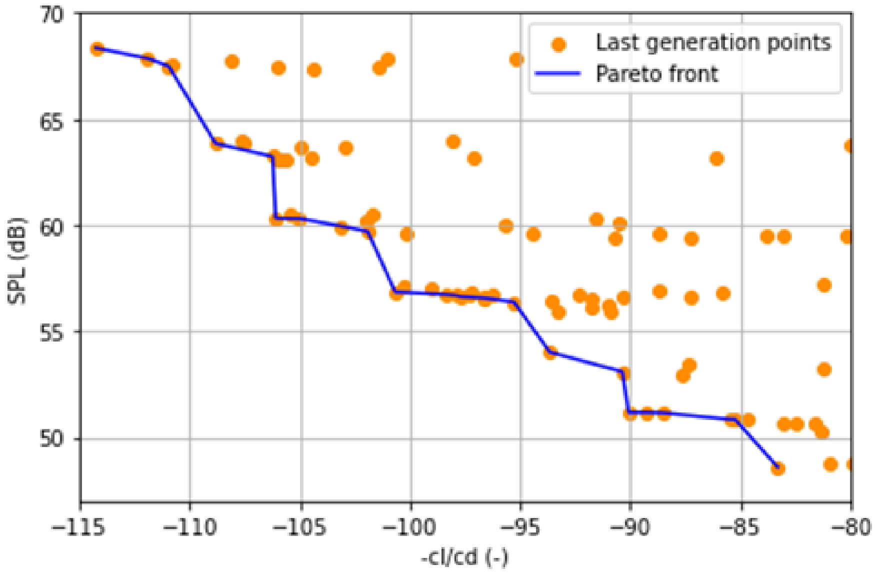

Figure 5.6: Pareto Front for Population size = 100, and Generation number=50.

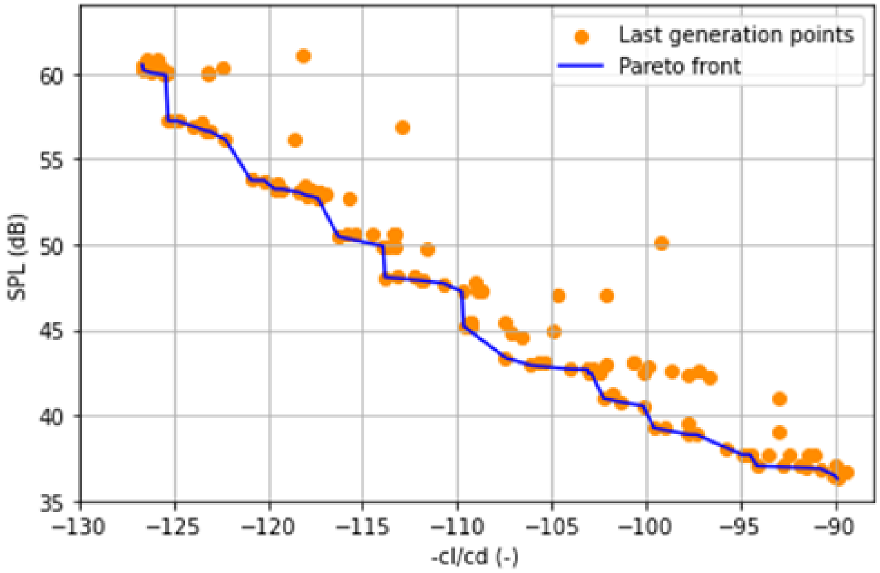

Figure 5.7: Pareto Front for Population size = 200, and Generation number=50.

When investigating the airfoil shapes optimized for minimized OASPL (Fig. 5.9) and maximized C_l/C_d (Fig. 5.8), a clear advancement is observed when compared with the outcomes of our first optimization phase described in 5.1. The airfoil optimized for C_l/C_d maximization (see Fig. 5.8) showcases a pronounced curvature increase at the TE, on the pressure side. This geometric modification plays an important role in securing an elevated lift coefficient.

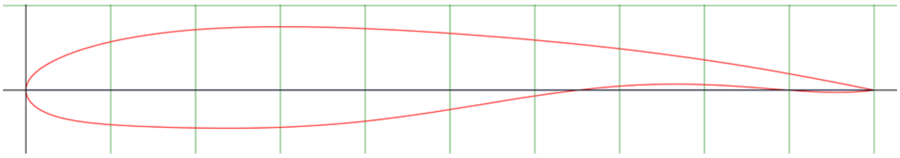

Figure 5.8: Airfoil shape optimized for maximum C_l/C_d

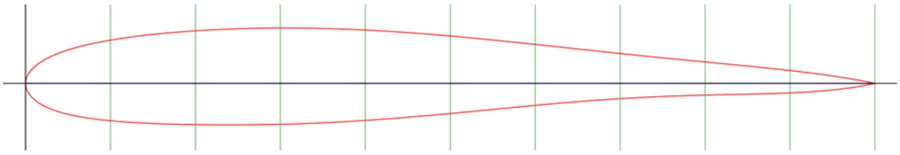

Figure 5.9: Airfoil shape optimized for minimum OASPL

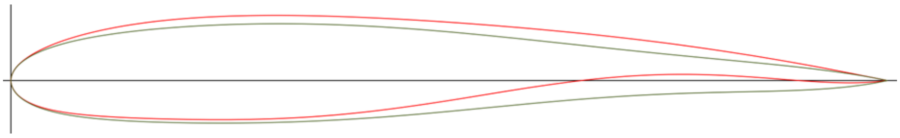

Figure 5.10: Comparison of the two optimized airfoils

Furthermore, the increased effectiveness of this second optimization approach is clearly demonstrated, as evidenced by Fig. 5.11. Observing the normalized values assumed by the nine design variables under optimized conditions reveals a notable improvement over the first optimization: the variable values are further away from the bounds, indicating a more effective optimization process.

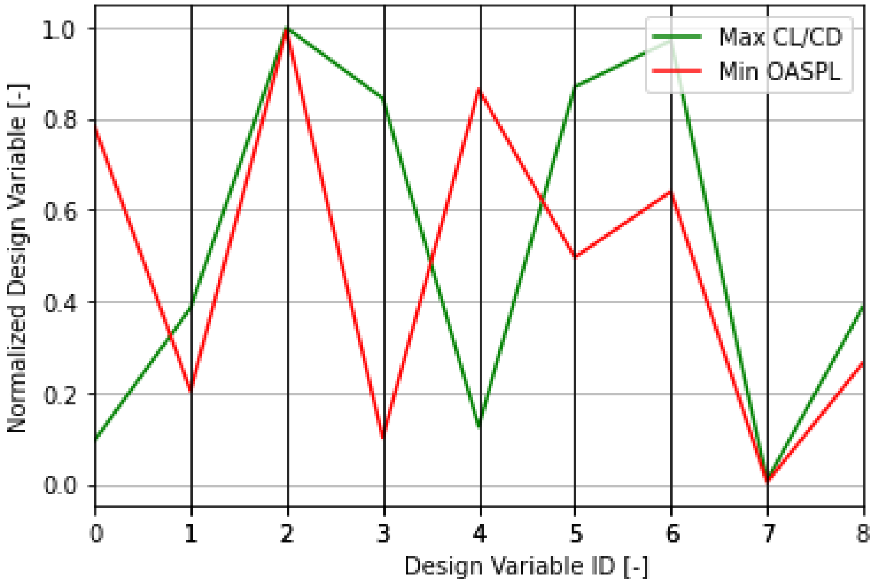

Figure 5.11: Normalized design variables value at optimized conditions

Further comparative analysis between the two optimized airfoils (see Fig. 5.10) reveals that, while the LE shapes show similarity, the shape modifications are evident at the TE, as expected for the reduction of TEN. This feature opens up to the possibility for research into airfoil morphing technologies. The possibility of engineering a morphing airfoil, capable of transitioning between these optimized shapes, offers a promising path to optimize performance across varying flight conditions. This adaptability could be very significant to achieve optimal aerodynamic efficiency and noise reduction across the flight envelope of the aircraft. On the down side, morphing technologies will add weight and complexity to the wing mechanism [94].

5.3. High fidelity evaluation

5.3.1. CFD results

The evaluation of the aerodynamic performance of the airfoil under study was carried out using RANS CFD simulations. Figures 5.12 and 5.13 illustrate the simulation results, focusing on the pressure coefficient distribution across the airfoil for the two distinct flight conditions, landing and cruise, respectively.

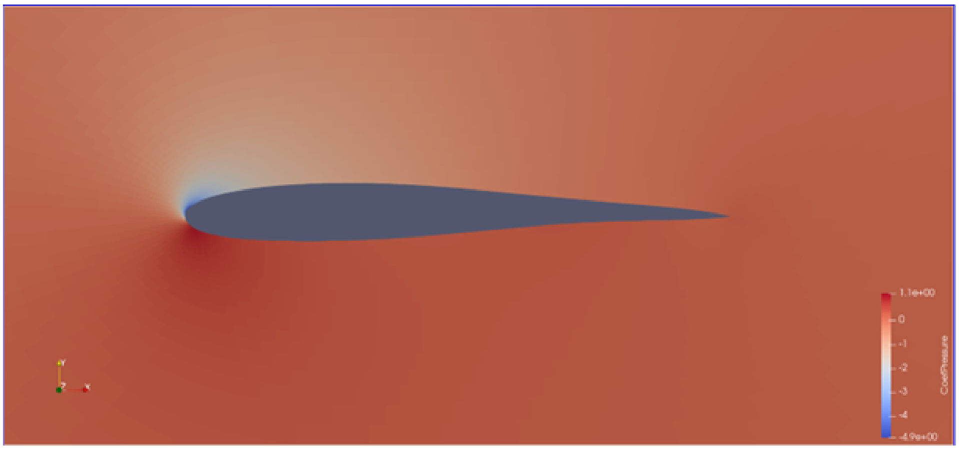

Figure 5.12: Pressure coefficient distribution at landing condition (M=0.2).

During the cruise condition, an abrupt and significant increase in the pressure coefficient is observed around the 50% chord position on the suction side of the airfoil profile (Figure 5.13). This phenomenon

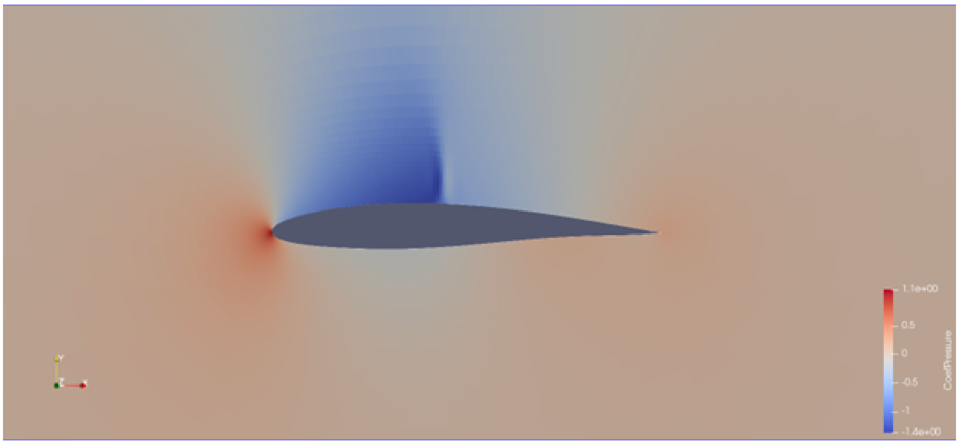

Figure 5.13: Pressure coefficient distribution at cruise condition (M= 0.7).

is attributed to the formation of a shockwave, which significantly impacts the airfoil's aerodynamic performance at high speeds.

A comparison of the pressure distributions obtained from the RANS simulations with those computed using the XFOIL solver reveals noteworthy differences, especially in their ability to predict the aerodynamic behavior under different flight conditions:

- For the landing case (see Fig. 5.15), the pressure distribution derived from both RANS simulations and XFOIL predictions exhibit remarkable similarity. However, XFOIL slightly overpredicts the peak pressure coefficient near the leading edge (LE) of the airfoil.

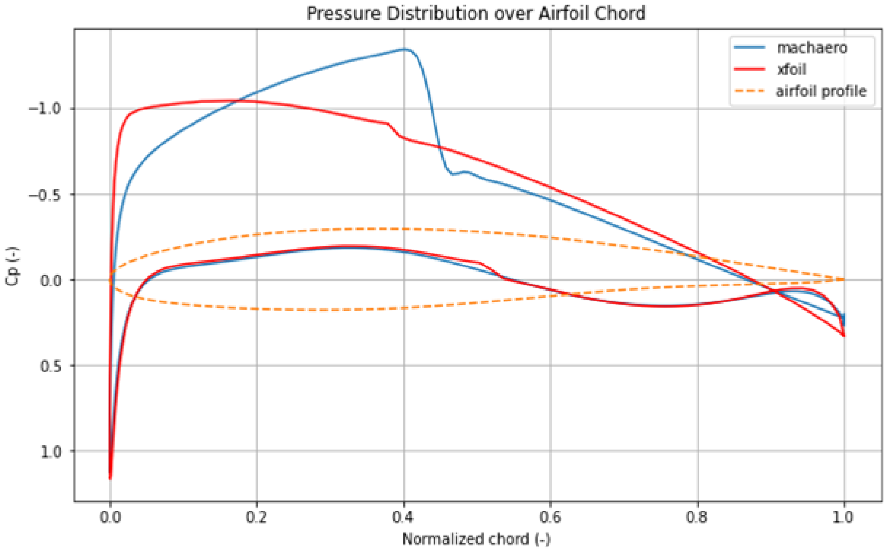

Figure 5.14: Pressure coefficient distribution of optimized airfoil at cruise conditions.

- In the cruise condition (see Fig. 5.14), the disparity between the two methods becomes more pronounced. The RANS simulation accurately captures the sharp increase in pressure due to the shockwave on the suction side, whereas XFOIL fails to picture this phenomenon. The pressure distribution according to XFOIL smoothly increases, demonstrating its limitation in characterizing the shockwave formation. This shortcoming of XFOIL significantly affects the accuracy of drag coefficient (C_d) calculations, as it does not account for the drag caused by the shockwave.

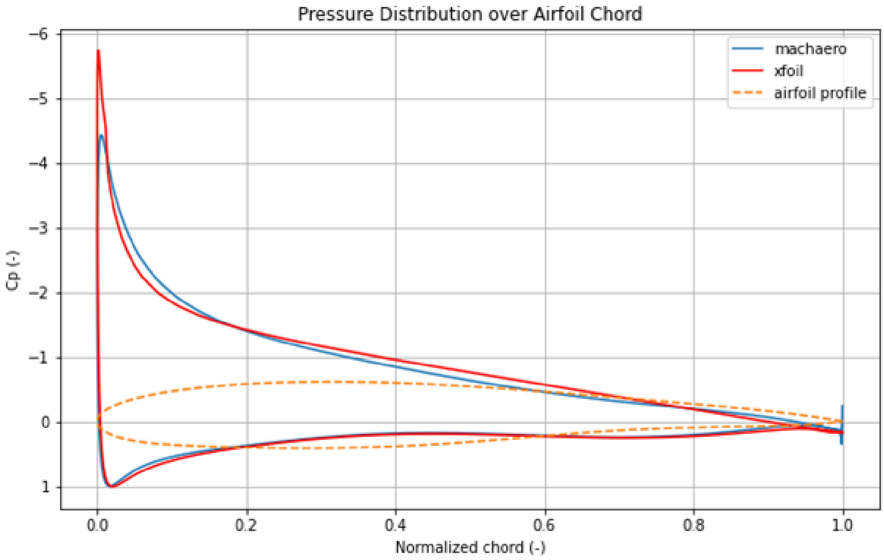

Figure 5.15: Pressure coefficient distribution of optimized airfoil at landing conditions.

The comparison of the lift and drag coefficient obtained with the two solvers is shown in Table 5.1. As it is shown, XFOIL is able to accurately compute the lift coefficient for both landing and cruise conditions, with a relative discrepancy of 0.66% and 3.71%, respectively. On the other hand, the drag prediciton shows the limitations of the low-fidelity solver. As it was mentioned, the inability of XFOIL to capture the shockwave at cruise speed results in 58.14% relative difference compared to the evaluation on ADFLOW (MachAero).

Table 5.1: Comparison of Solvers XFOIL and ADFLOW for Cruise and Landing Conditions

Condition	Coefficient	XFOIL	ADFLOW	Rel. Difference (%)
Cruise	C_l	0.597	0.62	3.71
	C_d	0.0054	0.0129	58.14
Landing	C_l	1.215	1.207	0.66
	C_d	0.011	0.013	15.38

These results highlight the importance of employing high-fidelity RANS CFD simulations for the accurate analysis of airfoil aerodynamics, particularly at high speeds where nonlinear phenomena become significant. The limitations of XFOIL, although useful for preliminary analyses, are evident in its inability to capture critical aerodynamic features that influence the performance of airfoils under cruise flight condition.

5.3.2. Aeroacoustic results

Having analyzed and compared the aerodynamic evaluations of the two different fidelities, we now advance our research by conducting a comparison of the aeroacoustic results derived from the TEN code, obtained using the boundary layer parameters extracted from XFOIL and RANS simulations. The comparison of SPL, relative to each frequency, is illustrated in Fig. 5.16.

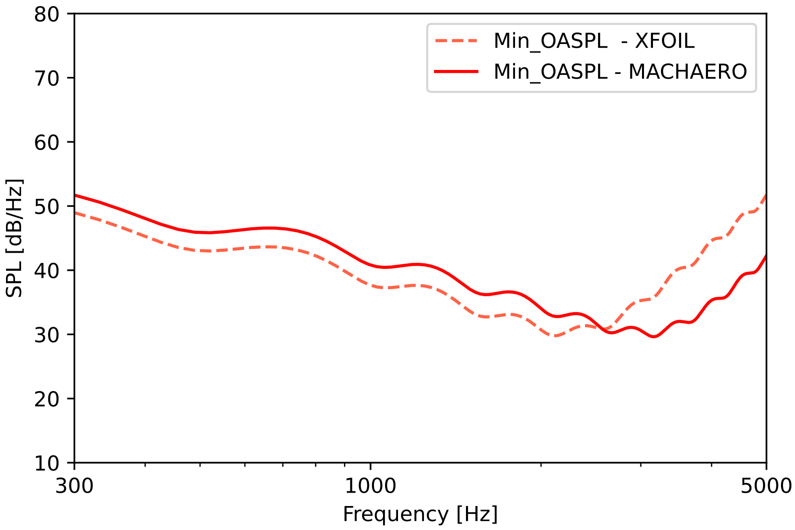

Figure 5.16: SPL comparison between results extracted with XFOIL and MACHAERO.

It is possible to see that the disparity between the solvers diminishes at lower frequencies. In scenarios involving frequencies above 1000Hz, which are relevant to our research for the calculation of the OASPL, the high fidelity prediction closely mirrors the trend observed in XFOIL up to about 3000Hz, beyond which it tends to be lower. Investigating the parameters that influence this trend (see Table 5.2), which are the TEN code input parameters derived by the aerodynamic simulations, we can see that XFOIL is able to accurately represent the external velocity U_e, as well as the boundary layer thickness (δ_{xx}) and the chordwise pressure gradient ($\frac{dp}{dx}$). On the other hand, the maximum normal shear stress τ_{max}, the momentum thickness θ and displacement thickness δ^* show some a significant discrepancy with the parameters extracted by ADFLOW.

Table 5.2: Boundary layer parameters comparison between XFOIL and ADFLOW

Parameter	**Unit**	**XFOIL**	**ADFLOW**	Δ (%)
U_e	m/s	0.96437	0.96704	$+0.28\%$
δ_{xx}	m	0.05079	0.05	-1.56%
δ^*	m	0.008465	0.005	-40.89%
θ	m	0.005	0.03333	$+566.60\%$
τ	Pa	3.41	2.6688	-21.76%
τ_{max}	Pa	3.41	7.2	$+111.14\%$
$\frac{dp}{dx}$	Pa/m	2115	2001	-5.39%
Re$_\theta$	-	22637	15091	-33.32%

5.3.3. Pareto Front high fidelity evaluation

As a next step, we extend the analysis conducted using the low-fidelity code, which integrated XFOIL with the TEN code, by employing a higher fidelity evaluation using RANS simulations. This entails re-evaluating each airfoil previously identified on the Pareto front to better understand their performance characteristics under more stringent simulation conditions.

Firstly, each airfoil on the low-fidelity Pareto front is subjected to a RANS simulation to assess its C_l and C_d. Additionally, we extract boundary layer parameters, and compute the corresponding TEN values. This process allows for a direct comparison of aerodynamic performance between the low and high fidelity models. The results are illustrated in Figure 5.17.

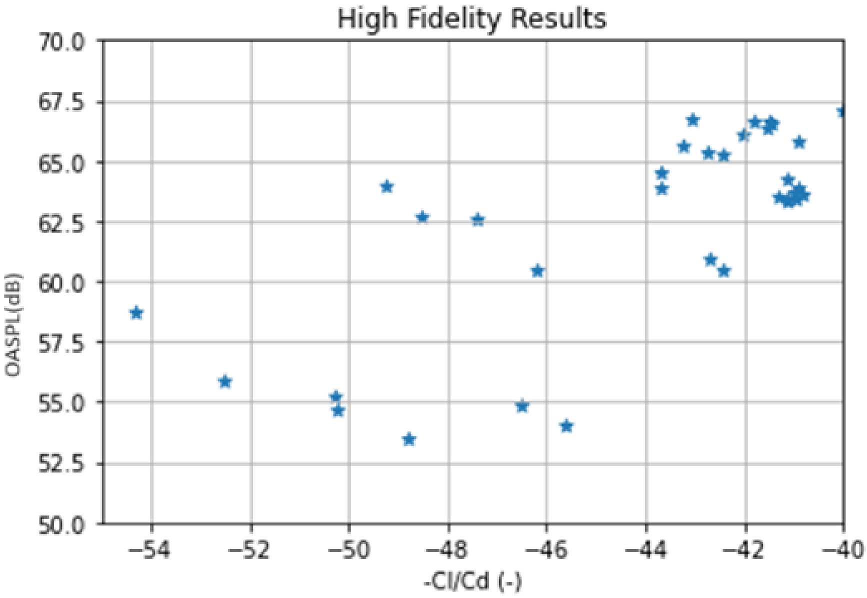

Figure 5.17: High fidelity evaluation of airfoils on the Pareto Front

It is evident from the figure that there is a notable reduction in the C_l/C_d ratios. This decrease primarily results from the increased drag coefficients in cruise conditions, which can be attributed to the formation of shockwaves, which are not captured by the lower fidelity simulations. Despite this, the emergence of a new Pareto front in the bottom left of the plot highlights regions where the airfoils still offer competitive trade-offs between lift and drag, even under more realistic flow conditions. A zoom into the newly formed Pareto front is shown in Fig. 5.18.

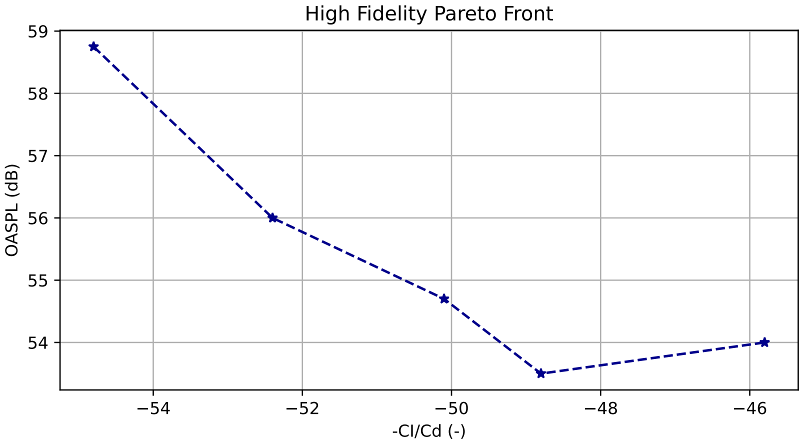

Figure 5.18: Pareto Front formed by the High Fidelity evaluation of the LF Pareto Front

We can observe that while the average C_l/C_d is decreased by 56.3% compared to the LF Pareto Front, the OASPL range between 53dB and 59dB, in line with the results obtained with the LF evaluation.

Furthermore, in Fig. 5.19 we can observe the airfoil shapes relative to the airfoil with maximum C_l/C_d and the one with minimum OASPL. Is is possible to see that the pressure side of the airfoil profile is quite comparable, while the airfoil optimized for high C_l/C_d presents less thickness especially between 30% and 80% chord, therefore decreasing the drag coefficient and increasing the aerodynamic efficiency. Furthermore, comparing these optimized shapes with the ones found with the LF evaluation (see Fig. 5.10), we can see that on the pressure side, next to the trailing edge, the airfoil present less curvature. This feature makes the airfoil shapes appealing for a potential implementation of a morphing technology, to transition from one optimized shape to another during flight.

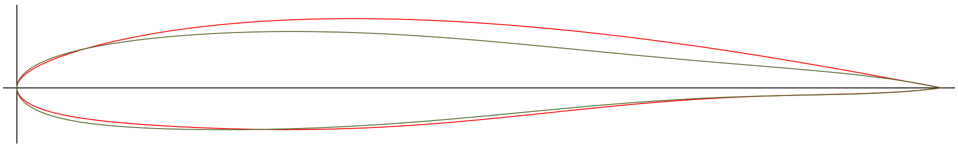

Figure 5.19: Optimized airfoil shape comparison: in green line, the airfoil presenting the highest C_l/C_d, in red the airfoil optimized for low OASPL.

Overall, this analysis confirms the value of high-fidelity simulations in capturing critical aerodynamic behaviors, thereby providing more accurate data for optimizing airfoil designs, especially at cruise condition.

6
Conclusions

This chapter serves as a final summary of the main findings and outcomes of this work. Section 6.1 outlines the primary findings derived from the research conducted and addresses the research questions introduced in Chapter 2. Furthermore, suggestions for future work are provided, emphasizing potential directions for additional exploration and proposing enhancements or advancements based on the acknowledged constraints of the present study.

6.1. Conclusions overview

This thesis addresses a pressing issue arising from the problems of increasing air traffic, urbanization, and the consequent rise in noise pollution generated by aircraft. The conventional approach to aeroacoustic optimization of an airfoil, often relegated to post-design noise reduction techniques, is no longer sustainable given the escalating demands for quieter air travel.

The primary objective of this study was to develop a multidisciplinary optimization methodology integrating aerodynamics and aeroacoustics to realize an airfoil optimized for both aerodynamic efficiency and minimal noise emission, particularly targeting Trailing Edge Noise (TEN). Through the development of a coupled aerodynamic-aeroacoustic optimization framework, employing a low computational cost TEN code grounded in Amiet theory, and coupling it with XFOIL or AFLOW aerodynamic solvers, we aimed to explore the trade-off between aerodynamic performance during cruise and noise emission during landing.

Our optimization results, produced by the NSGA-II algorithm, yielded promising results manifested in clear Pareto fronts, showing optimized airfoil configurations with an optimal balance between aerodynamic efficiency and noise reduction. Thanks to the efficiency of XFOIL and the TEN code, we successfully executed the multi-objective optimization, demonstrating the viability of our approach within reasonable computational timeframes.

Verification of our optimized designs through high-fidelity RANS CFD simulations on ADFLOW confirmed the efficacy of our low-fidelity framework, particularly in capturing aeroacoustic performance during landing conditions. However, it is acknowledged that at higher Mach numbers, characterized by cruise conditions, the limitations of XFOIL become apparent due to its inability to account for phenomena such as wave drag induced by shockwaves. Consequently, for investigations into cruise conditions, recourse to higher-fidelity aerodynamic analyses becomes imperative.

Nonetheless, the demonstrated efficiency and reliability of our low-fidelity framework endorse its applicability as a standalone tool for scenarios characterized by Mach numbers up to 0.5, where shockwave-induced phenomena are not present. This underscores the versatility and practicality of our approach in real-world applications, offering a promising avenue for the design of quieter and more efficient airfoils to mitigate the adverse impacts of aeronautical noise pollution in urbanized environments.

6.1.1. Research Questions

In this section, we address the initial goals and research questions set forth at the beginning of this work, drawing upon the insights gained from our study and the conclusions derived from our findings.

1. **Addressing the Dual Challenge of Aerodynamics and Aeroacoustics Optimization**: The main research question posed at the beginning of this work was: *How can we simultaneously minimize drag and noise in the aerodynamic design of an airfoil?* In addition, the exploration of aerodynamic and aeroacoustic optimization uncovered the challenge posed by the high computational cost associated with unsteady simulations for noise prediction. In order to tackle this, the present study made use of a coupled framework based on two low fidelity and computational efficient solvers: XFOIL for the aerodynamics and a TEN Amiet code for the aeroacoustics. This coupling proved to be not only effective in terms of computational cost, but also provided a good baseline for the coupled optimization, producing defined Pareto fronts and optimized airfoils with promising characteristics.
2. **Comparative Analysis of Lower and Higher Fidelity Solvers**: In order to verify the results of the low fidelity framework, a comparative analysis between the lower and higher fidelity solvers was executed, dealing with both the aerodynamic and aeroacoustic parts. Regarding the first point, it was evident that XFOIL proved to be reliable at landing conditions, namely at low Mach number and high angle of attack. For the cruise conditions, despite an accurate lift coefficient prediction, XFOIL proved to strongly underestimate the drag compared to the higher fidelity RANS CFD. This is, as mentioned, due to the presence of shock waves that XFOIL is not able to capture. Regarding the aeroacoustic results, these were extracted from the same TEN code, run with different inputs from the LF or HF aerodynamic code.

   Given the smaller relative differences between the two aerodynamic solvers for the landing scenario, the results are closer; however, the HF solver is showing a lower estimation of OASPL compared to the LF solver, which for the reference case of NACA0012 tended to overpredict the OASPL. With this in consideration, we can assert that the HF solver provides promising results, which will need to be validated with experimental data in future research.
3. **Optimization at Various Flight Conditions**: Expanding upon existing research, our study conducted the optimization of the 2D airfoil under diverse flight conditions, including different Mach numbers, Reynolds numbers, and angles of attack. With this comprehensive assessment, we were able to investigate the performance of the airfoil across the flight envelope, targeting our objective function towards the most relevant condition: to maximize C_l/C_d at cruise conditions, while minimizing the OASPL at landing, when the aircraft is in closer proximity to urban areas, and the engines are in low power setting. This multi-point research is relevant to develop more efficient and potentially adaptable airfoil designs, with the use of morphing technologies.

In addressing these research questions, our study contributed to the broader body of knowledge in aerodynamic and aeroacoustic optimization, offering insights and methodologies that have the potential to shape the future of aircraft design and operation.

6.2. Future Work

For future recommendations, several paths emerge from the findings and limitations of this study, offering opportunities for further research and refinement of the proposed optimization framework.

1. **Integration of High-Fidelity Evaluation**: To enhance the accuracy of multi-point optimization while managing computational costs, integrating high-fidelity evaluations, such as RANS simulations, directly into the optimization process is a promising direction. By blending the low-fidelity XFOIL with higher-fidelity RANS simulations in a multi-fidelity optimization framework, we can leverage the strengths of both approaches to achieve more accurate and robust results across a range of operating conditions, particularly at cruise conditions where the low fidelity solver proved ineffective.
2. **Application to Different Mach Numbers and Validation**: Extending the application of the optimization framework to a wider range of Mach numbers and diverse aerodynamic scenarios represents another recommendation for future research. Testing the framework across lower Mach numbers and different operational conditions would provide a comprehensive assessment of its versatility and effectiveness. Additionally, validating the optimized designs through experimental testing, such as wind tunnel experiments or flight trials, would validate the accuracy and applicability of the proposed methodology in real-world settings.

3. **Exploration of Morphing Wing Concepts**: Building upon the optimized airfoil designs generated in this study, future research could use this work to explore the feasibility and benefits of implementing morphing wing technologies. By dynamically adjusting the airfoil shape between configurations optimized for low OASPL and maximum C_l/C_d, morphing wings offer the potential to further enhance both aerodynamic efficiency and noise reduction across different flight phases. Investigating the practicalities and performance implications of such morphing wing designs could yield valuable insights into the integration of adaptive aerodynamic solutions for next-generation aircraft.

By pursuing these future recommendations, researchers can advance the state-of-the-art in aerodynamic and aeroacoustic optimization, setting the path for the development of quieter, more efficient airfoil designs that address the challenges of urban air mobility and sustainable aviation.

References

1. Organization, W. H. Burden of disease from environmental noise. Quantification of healthy life years lost in Europe. *Technical report, JRC European Commission, Copenhagen, Denmark* (2011).
2. Jarup, L. *et al.* Hypertension and Exposure to Noise Near Airports: the HYENA Study. *Environmental Health Perspectives* **116,** 329–333. eprint: `https://ehp.niehs.nih.gov/doi/pdf/10.1289/ehp.10775`. `https://ehp.niehs.nih.gov/doi/abs/10.1289/ehp.10775` (2008).
3. Clark, C., Head, J. & Stansfeld, S. A. Longitudinal effects of aircraft noise exposure on children's health and cognition: A six-year follow-up of the UK RANCH cohort. *Journal of Environmental Psychology* **35,** 1–9. ISSN: 0272-4944. `https://www.sciencedirect.com/science/article/pii/S027249441300011X` (2013).
4. Egbenta, I. R., Uchegbu, S. N., Ubani, E. & Akalemeaku, O. J. Effects of Noise Pollution on Residential Property Value in Enugu Urban, Nigeria. *SAGE Open* **11,** 21582440211032167 (2021).
5. Babisch, W. Cardiovascular Effects of Noise (ed Nriagu, J.) 532–542. `https://www.sciencedirect.com/science/article/pii/B9780444522726002440` (2011).
6. United Nations, D. o. E. & Affairs, S. World Urbanization Prospects: The 2014 Revision. *Population Division, New York* (2015).
7. Airbus. Global Market Forecast. Growing Horizons 2017/2036. *Technical Report, Airbus S.A.S., Blagnac Cedex, France* (2017).
8. Boeing. Current Market Outlook 2017/2036. *Technical report, Boeing, Seattle. WA 98124-2207.*
9. Girvin, R. Aircraft noise-abatement and mitigation strategies. *Journal of Air Transport Management* **15,** 14–22. ISSN: 0969-6997. `https://www.sciencedirect.com/science/article/pii/S0969699708001166` (2009).
10. (ICAO), I. C. A. O. Annex 16 Environmental Protection Volume I, 9th edition (2014).
11. For Aviation Research, A. C. & in Europe (ACARE), I. Flight-path 2050. `https://www.acare4europe.org/acare-goals/`.
12. (FAA), F. A. A. Continuous Lower Energy, Emissions, and Noise (CLEEN) Program. `https://www.faa.gov/about/office_org/headquarters_offices/apl/eee/technology_saf_operations/cleen`.
13. Association, I. A. T. *Sustainability and Economics, Tourism Economics* in (2023).
14. Ibren, M., Andan, A. D., Asrar, W. & Sulaeman, E. A Review on Generation and Mitigation of Airfoil Self-Induced Noise. *Journal of Advanced Research in Fluid Mechanics and Thermal Sciences* **90,** 163–178 (2022).
15. Amirsalari, B. & Rocha, J. Recent Advances in Airfoil Self-Noise Passive Reduction. *Aerospace* **10,** 791 (2023).
16. Masters, D. Review of Aerofoil Parameterisation Methods for Aerodynamic Shape Optimisation. *AIAA SciTech.* DOI: 10.2514/6.2015-0761 (2015).
17. Kulfan, B. A Universal Parametric Geometry Representation Method – "CST". *AIAA* (2007).
18. Sederberg, T. W. & Parry, S. R. Free-Form Deformation of Solid Geometric Models. *SIGGRAPH Comput. Graph.* **20,** 151–160. ISSN: 0097-8930. `https://doi.org/10.1145/15886.15903` (Aug. 1986).
19. Derksen, R. & Rogalsky, T. Bezier-PARSEC: An optimized aerofoil parameterization for design. *Advances in engineering software* **41,** 923–930 (2010).
20. Sobieczky, H. *Parametric Airfoils and Wings* 71–88 (K. Fujii, G.S. Dulikravich (Ed.): Notes on Numerical Fluid Mechanics, Vol.68, Vieweg Verlag, 1998).

21. Samareh, J. A. Survey of shape parameterization techniques for high-fidelity multidisciplinary shape optimization. *AIAA journal* **39,** 877–884 (2001).
22. Della Vecchia, P., Daniele, E. & D'Amato, E. An airfoil shape optimization technique coupling PARSEC parameterization and evolutionary algorithm. *Aerospace Science and Technology* **32,** 103–110 (2014).
23. Hicks, R. M. & Henne, P. A. Wing design by numerical optimization. *Journal of Aircraft* **15,** 407–412 (1978).
24. Skinner, S. & Zare-Behtash, H. State-of-the-art in aerodynamic shape optimisation methods. *Applied Soft Computing* **62,** 933–962. ISSN: 1568-4946. `https://www.sciencedirect.com/science/article/pii/S1568494617305690` (2018).
25. Nocedal, J. & Wright, S. J. *Numerical optimization* (Springer, 1999).
26. Sobieszczanski-Sobieski, J. & Haftka, R. T. Multidisciplinary aerospace design optimization: survey of recent developments. *Structural optimization* **14,** 1–23 (1997).
27. Jameson, A. Aerodynamic design via control theory. *Journal of scientific computing* **3,** 233–260 (1988).
28. Martins, J. R. Aerodynamic design optimization: Challenges and perspectives. *Computers & Fluids* **239,** 105391 (2022).
29. Halila, G. L., Martins, J. R. & Fidkowski, K. J. Adjoint-based aerodynamic shape optimization including transition to turbulence effects. *Aerospace Science and Technology* **107,** 106243 (2020).
30. Abergo, L., Morelli, M. & Guardone, A. Aerodynamic shape optimization based on discrete adjoint and RBF. *Journal of Computational Physics* **477,** 111951 (2023).
31. Gibert Martínez, I., Afonso, F., Rodrigues, S. & Lau, F. A sequential approach for aerodynamic shape optimization with topology optimization of airfoils. *Mathematical and Computational Applications* **26,** 34 (2021).
32. Antunes, A. P. & Azevedo, J. L. F. Studies in aerodynamic optimization based on genetic algorithms. *Journal of Aircraft* **51,** 1002–1012 (2014).
33. Holland, J. Adaptation in Natural and Artificial Systems. ann arbor: University of michigan press. *Ann Arbor: The University of Michigan Press* (1975).
34. Deb, K., Pratap, A., Agarwal, S. & Meyarivan, T. A fast and elitist multiobjective genetic algorithm: NSGA-II. *IEEE transactions on evolutionary computation* **6,** 182–197 (2002).
35. Arias-Montano, A., Coello Coello, C. A. & Mezura-Montes, E. Evolutionary algorithms applied to multi-objective aerodynamic shape optimization. *Computational optimization, methods and algorithms,* 211–240 (2011).
36. Chang, Y., Bouzarkouna, Z. & Devegowda, D. Multi-objective optimization for rapid and robust optimal oilfield development under geological uncertainty. *Computational Geosciences* **19,** 933–950 (June 2015).
37. Martinez, R. V. On the Design of a Methodology for Camber Morphing Optimisation with Noise Reduction. *Instituto Superior Tecnico (IST)* (2019).
38. B.Zhou T.Albring, N. G. Efficient Airframe Noise Reduction Framework via Adjoint-Based Shape Optimization. *AIAA Journal* **59,** 580–595 (2021).
39. T.D. Economon F.Palacios, J. A. A Coupled-Adjoint Method for Aerodynamic and Aeroacoustic Optimization. *12th AIAA Aviation Technology, Integration and Operations Conference and 14th AIAA/ISSM* (2012).
40. M.A. Moratilla-Vega M. Angelino, H. X. & Page, G. An open-source coupled method for aeroacoustics modelling. *Computer Physics Communications* (2022).
41. Moratilla-Vega, M., Lackhove, K., Janicka, J., Xia, H. & Page, G. Jet noise analysis using an efficient LES/high-order acoustic coupling method. *Computers & Fluids* **199,** 104438 (2020).
42. Zhou, B. Y., Gauger, N. R., Satcunanathan, S., Meinke, M. H. & Schroeder, W. in *AIAA Scitech 2020 Forum* (). eprint: `https://arc.aiaa.org/doi/pdf/10.2514/6.2020-1727`. `https://arc.aiaa.org/doi/abs/10.2514/6.2020-1727`.

43. Blonigan, P., Chen, R., Wang, Q. & Larsson, J. *Towards adjoint sensitivity analysis of statistics in turbulent flow simulation* in *Proceedings of the Summer Program* (2012), 229.
44. Zhou, B. *et al. Reduction of airframe noise components using a discrete adjoint approach* in *18th AIAA/ISSMO multidisciplinary analysis and optimization conference* (2017), 3658.
45. Volkmer, K. & Carolus, T. *Aeroacoustic airfoil shape optimization utilizing semi-empirical models for trailing edge noise prediction* in *2018 AIAA/CEAS aeroacoustics conference* (2018), 3130.
46. Drela, M. *XFOIL: An analysis and design system for low Reynolds number airfoils* in *Low Reynolds Number Aerodynamics: Proceedings of the Conference Notre Dame, Indiana, USA, 5–7 June 1989* (1989), 1–12.
47. Kamruzzaman, M., Bekiropoulos, D., Lutz, T., Würz, W. & Krämer, E. A semi-empirical surface pressure spectrum model for airfoil trailing-edge noise prediction. *International journal of aeroacoustics* **14,** 833–882 (2015).
48. Amiet, R. K. Noise due to turbulent flow past a trailing edge. *Journal of sound and vibration* **47,** 387–393 (1976).
49. Ricks, N., Tsirikoglou, P., Contino, F. & Ghorbaniasl, G. *A CFD-based methodology for aerodynamic-aeroacoustic shape optimization of airfoils* in *AIAA Scitech 2020 Forum* (2020), 1729.
50. Küçükosman, Y. C., Christophe, J. & Schram, C. Trailing edge noise prediction based on wall pressure spectrum models for NACA0012 airfoil. *Journal of Wind Engineering and Industrial Aerodynamics* **175,** 305–316 (2018).
51. Lee, S. Empirical wall-pressure spectral modeling for zero and adverse pressure gradient flows. *AIAA Journal* **56,** 1818–1829 (2018).
52. Ripepi, M. *et al.* Reduced-order models for aerodynamic applications, loads and MDO. *CEAS Aeronautical Journal* **9,** 171–193 (2018).
53. Yao, W., Marques, S., Robinson, T., Armstrong, C. & Sun, L. A reduced-order model for gradient-based aerodynamic shape optimisation. *Aerospace Science and Technology* **106,** 106120 (2020).
54. M.G. Fernandez-Godino C. Park, N. K. & Haftka, R. Review of multi-fidelity models (2012).
55. Serani, A. *et al.* Adaptive multi-fidelity sampling for CFD-based optimisation via radial basis function metamodels. *International Journal of Computational Fluid Dynamics* **33,** 237–255 (2019).
56. J. Li X. Du, J. M. Machine learning in aerodynamic shape optimization. *Progress in Aerospace Sciences 134.* https://doi.org/10.1016/j.paerosci.2022.100849 (2022).
57. D.J. Lucia P.S. Beran, W. S. Reduced-order modeling: new approaches for computational physics. *Progress in Aerospace Sciences* **40.** doi:10.1016/j.paerosci.2003.12.001, 51–117 (2004).
58. F. Salmoiraghi A. Scardigli, H. T. & Rozza, G. Free-form deformation, mesh morphing and reduced-order methods: enablers for efficient aerodynamic shape optimisation. *International Journal of Computational Fluid Dynamics* **32.** https://doi.org/10.1080/10618562.2018.1514115, 233–247 (2018).
59. M.Buffoni H. Telib, A. I. Iterative Methods for Model Reduction by Domain Decomposition. *Computers and Fluids* **38,** 1160–1167 (2009).
60. V. Raul, L. L. Surrogate-based aerodynamic shape optimization for delaying airfoil dynamic stall using Kriging regression and infill criteria. *Aerospace Science and Technology* **111.** https://doi.org/10.1016/j.ast.202 (2021).
61. M.D. McKay R.J. Beckman, W. C. A comparison of three methods for selecting values of input variables in the analysis of output from a computer code. *Technometrics* **42.** 10.1080/00401706.2000.10485979, 55–61 (2000).
62. Demiral, E., Sahin, C. & Arslan, K. *Aerodynamic Shape Optimization Using Multi-fidelity Surrogate-based Approach for Computationally Expensive Problems* in *AIAA AVIATION 2022 Forum* (2022), 4161.
63. Liu, H., Ong, Y.-S. & Cai, J. A survey of adaptive sampling for global metamodeling in support of simulation-based complex engineering design. *Structural and Multidisciplinary Optimization* **57,** 393–416 (2018).
64. Anderson Jr, J. D. Fundamentals of Aerodynamics, McGraw-Hill. *New York* (1991).

65. Abbott, I. H. & Von Doenhoff, A. E. *Theory of wing sections: including a summary of airfoil data* (Courier Corporation, 2012).
66. Leishman, J. G. *Introduction to Aerospace Flight Vehicles* (Embry-Riddle Aeronautical University, 2023).
67. Morgado, J., Vizinho, R., Silvestre, M. & Páscoa, J. XFOIL vs CFD performance predictions for high lift low Reynolds number airfoils. *Aerospace Science and Technology* **52,** 207–214 (2016).
68. Van Ingen, J. *The eN method for transition prediction. Historical review of work at TU Delft* in *38th Fluid Dynamics Conference and Exhibit* (2008), 3830.
69. Rogers, S., Menter, F., Durbin, P. & Mansour, N. *A comparison of turbulence models in computing multi-element airfoil flows* in *32nd Aerospace Sciences Meeting and Exhibit* (1994), 291.
70. Valarezo, W. O. & Mavriplis, D. J. Navier-Stokes applications to high-lift airfoil analysis. *Journal of aircraft* **32,** 618–624 (1995).
71. Godin, P., Zingg, D. & Nelson, T. High-lift aerodynamic computations with one-and two-equation turbulence models. *AIAA journal* **35,** 237–243 (1997).
72. Nguyen, C. Turbulence modeling. *MIT* **1,** 1–6 (2005).
73. Allmaras, S. R. & Johnson, F. T. *Modifications and clarifications for the implementation of the Spalart-Allmaras turbulence model* in *Seventh international conference on computational fluid dynamics (ICCFD7)* **1902** (2012).
74. Wilcox, D. C. *et al. Turbulence modeling for CFD* (DCW industries La Canada, CA, 1998).
75. Lee, S. *et al.* Turbulent boundary layer trailing-edge noise: Theory, computation, experiment, and application. *Progress in Aerospace Sciences* **126,** 100737 (2021).
76. Fethney, P. *American Institute of Aeronautics and Astronautics Paper No. 75-511* 1975.
77. Hardin, J. C. *Airframe self-noise: Four years of research* tech. rep. (1976).
78. Brooks, T. F. & Hodgson, T. Trailing edge noise prediction from measured surface pressures. *Journal of sound and vibration* **78,** 69–117 (1981).
79. Powell, A. On the aerodynamic noise of a rigid flat plate moving at zero incidence. *The Journal of the Acoustical Society of America* **31,** 1649–1653 (1959).
80. Lighthill, M. J. On sound generated aerodynamically I. General theory. *Proceedings of the Royal Society of London. Series A. Mathematical and Physical Sciences* **211,** 564–587 (1952).
81. Williams, J. F. & Hall, L. Aerodynamic sound generation by turbulent flow in the vicinity of a scattering half plane. *Journal of fluid mechanics* **40,** 657–670 (1970).
82. Howe, M. S. A review of the theory of trailing edge noise. *Journal of sound and vibration* **61,** 437–465 (1978).
83. Noble, B. & Weiss, G. Methods based on the Wiener-Hopf technique for the solution of partial differential equations. *Physics Today* **12,** 50–50 (1959).
84. Roger, M. & Moreau, S. Back-scattering correction and further extensions of Amiet's trailing-edge noise model. Part 1: theory. *Journal of Sound and vibration* **286,** 477–506 (2005).
85. Mader, C. A., Kenway, G. K., Yildirim, A. & Martins, J. R. ADflow: An open-source computational fluid dynamics solver for aerodynamic and multidisciplinary optimization. *Journal of Aerospace Information Systems* **17,** 508–527 (2020).
86. Skinner, S. N. & Zare-Behtash, H. State-of-the-art in aerodynamic shape optimisation methods. *Applied Soft Computing* **62,** 933–962 (2018).
87. Blank, J. & Deb, K. Pymoo: Multi-objective optimization in python. *Ieee access* **8,** 89497–89509 (2020).
88. Versteeg, H. K. *An introduction to computational fluid dynamics the finite volume method, 2/E* (Pearson Education India, 2007).
89. Secco, N. R., Kenway, G. K., He, P., Mader, C. & Martins, J. R. Efficient mesh generation and deformation for aerodynamic shape optimization. *AIAA Journal* **59,** 1151–1168 (2021).

90. Spalart, P. & Allmaras, S. *A one-equation turbulence model for aerodynamic flows* in *30th aerospace sciences meeting and exhibit* (1992), 439.

91. Yildirim, A., Kenway, G. K., Mader, C. A. & Martins, J. R. A Jacobian-free approximate Newton–Krylov startup strategy for RANS simulations. *Journal of Computational Physics* **397,** 108741 (2019).

92. Rozenberg, Y., Robert, G. & Moreau, S. Wall-pressure spectral model including the adverse pressure gradient effects. *AIAA journal* **50,** 2168–2179 (2012).

93. Deb, K., Sindhya, K. & Hakanen, J. in *Decision sciences* 161–200 (CRC Press, 2016).

94. Sofla, A., Meguid, S., Tan, K. & Yeo, W. Shape morphing of aircraft wing: Status and challenges. *Materials & Design* **31,** 1284–1292 (2010).